Journal of Fluids and Structures 76 (2018) 95–115

Contents lists available at ScienceDirect

Journal of Fluids and Structures

journal homepage: www.elsevier.com/locate/jfs

Control of low Reynolds number flow around an airfoil using periodic surface morphing: A numerical study

Gareth Jones [a,b], Matthew Santer [a], George Papadakis [a,*]

[a] Department of Aeronautics, Imperial College London, SW7 2AZ, UK
[b] Department of Mechanical Engineering, National University of Singapore, 117608, Singapore

ARTICLE INFO

Article history:
Received 31 March 2017
Received in revised form 29 July 2017
Accepted 25 September 2017

Keywords:
Direct numerical simulations
Separation control
Surface morphing
Low Reynolds numbers
Aerodynamics

ABSTRACT

The principal aim of this paper is to use Direct Numerical Simulations (DNS) to explain the mechanisms that allow periodic surface morphing to improve the aerodynamic performance of an airfoil. The work focuses on a NACA-4415 airfoil at Reynolds number $Re_c = 5 \times 10^4$ and 0° angle of attack. At these flow conditions, the boundary layer separates at $x/c = 0.42$, remains laminar until $x/c \approx 0.8$, and then transitions to turbulence. Vortices are formed in the separating shear layer at a characteristic Kelvin–Helmholtz frequency of $St_s = 4.9$, which compares well with corresponding experiments. These are then shed into the wake. Turbulent reattachment does not occur because the region of high turbulent kinetic energy (and therefore mixing) is located too far downstream and too far away from the airfoil surface to influence the near-wall flow. The effect of three actuation frequencies is examined by performing the simulations on a computational domain that deforms periodically. It is found that by amplifying the Kelvin–Helmholtz instability mechanism, Large Spanwise Coherent structures are forced to form and retain their coherence for a large part of the actuation cycle. Following their formation, these structures entrain high momentum fluid into the near-wall flow, leading to almost complete elimination of the recirculation zone. The instantaneous and phase averaged characteristics of these structures are analyzed and the vortex coherence is related to the phase of actuation. In order to further clarify the process of reduction in the size of recirculation zone, simulations start from the fully-developed uncontrolled flow and continue for 25 actuation cycles. The results indicate that the modification of airfoil characteristics is a gradual process. As the number of cycles increases and the coherent vortices are repeatedly formed and propagate downstream, they entrain momentum, thereby modifying the near wall region. During this transient period, the separated shear layer approaches the airfoil surface and the size of recirculation region decreases. It takes at least 15 cycles for the flow to develop a repeatable, periodic pattern.

1. Introduction

Civilian and military interest in Micro and Unmanned Air Vehicles (MAVs and UAVs respectively) has increased significantly in recent years. These vehicles can carry very small sensors, video cameras, listening devices and control hardware systems and they are capable of complex missions ranging from surveillance and communication relay to detection

* Corresponding author.
E-mail address: g.papadakis@ic.ac.uk (G. Papadakis).

https://doi.org/10.1016/j.jfluidstructs.2017.09.009

of biological, chemical, or nuclear materials (Mueller and DeLaurier, 2003). The combination of small length scales and low velocities results in an operating flight regime of Re_c in the range of 15,000 to 500,000.

At such Reynolds numbers, a laminar boundary layer forms on an airfoil's upper surface and persists beyond the suction peak and into the pressure recovery region, where it encounters an adverse pressure gradient. Viscous effects close to the wall slow down a fluid element, thereby reducing its kinetic energy. Turbulent boundary layers can entrain higher momentum fluid from the edge of the boundary layer and mix it effectively with lower momentum fluid close to the surface, thus energizing the near-wall region. In laminar boundary layers this mechanism is much slower and the energy of the near-wall flow remains very low. This makes them incapable of overcoming even modest adverse pressure gradients and prone to separation even at low angles of attack, resulting in high drag and loss of lift (Mcmasters and Henderson, 1979; Mueller and Batil, 1982; Laitone, 1997; Marchman and Abtahi, 1985; Wang et al., 2014).

Flow control can counter such unfavorable behavior and potentially lead to considerable performance improvements. Given an imposed pressure field, the principle strategy in separation control is to add momentum to the very near-wall region. Passive flow control techniques, like Vortex Generators (VG) (Kerho et al., 1993; Abbas et al., 2013; Lin, 2002) or surface roughness (Zhou and Wang, 2012; Mueller and Batil, 1982; Greenblatt and Wygnanski, 2000) are easily implemented, but their performance is optimal only at design conditions. An aircraft would encounter a variety of flow conditions during a single mission, thus it is doubtful whether such control strategies can have a net positive effect in practice.

In contrast, active control approaches remove the drawback associated with passive control at off-design conditions. This form of control has been associated mainly with periodic injection or suction of fluid from a boundary layer. Periodic forcing was first used by Schubauer and Skramstad (1948) who introduced periodic perturbations in a laminar boundary layer to trigger a known instability (the Tollmien–Schlichting wave). More recently, the most widely researched periodic active flow control methods are Synthetic Jets (or Zero-Net-Mass-Flux jets) (Kotapati et al., 2010; Buchmann et al., 2013; Zhang and Samtaney, 2015; Amitay et al., 2001) and Direct-Barrier-Discharge (DBD) Plasma actuators (Sato et al., 2015). The formation of Large Coherent Structures (LCS) in the separated shear layer has been widely observed (Kotapati et al., 2010; Yarusevych et al., 2009) and the periodic actuation is believed to be capable of accelerating and regulating their production. These structures are the essential 'building blocks' of the mixing layer (Greenblatt and Wygnanski, 2000) and are responsible for transporting momentum across it. The triggering of LCS is therefore an efficient method for control of mixing in the separated shear layer and consequently, periodic actuation can increase the transfer of high momentum fluid, enhancing entrainment. This principle forms the basis of separation control by periodic excitation. Since the effectiveness of the method is largely determined by the receptivity of the flow to the imposed disturbances, these have to be of the right scale and be introduced at the right location. The control authority of periodic excitation has been found to exhibit a highly non-monotonic variation with actuation frequency which suggests the presence of rich flow physics (Kotapati et al., 2010). Benard and Moreau (2011) investigated experimentally the use of DBD plasma actuators for separation control. When the actuator was activated in an initially quiescent flow field, it produced a large counter-clockwise rotating vortex. However, no such vortex was observed when used in the actual flow, but instead an amplification of a clockwise rotating LCS was found. The velocity of the gas produced by the actuator alone was one order of magnitude lower than the external velocity, but still produced a dramatic effect. In agreement with what was stated above, this led the authors to conclude that the momentum transfer did not come from the actuator directly but the actuator instead acted as a catalyzer that reinforced an already existing instability.

Many numerical simulations have been reported in the literature to elucidate the effect of periodic actuation on the separation flow characteristics. Postl et al. (2011) used Direct Numerical Simulations to investigate pulsed vortex generator jets (pVGJ) for separation control. They also observed the production of LCS and were able to confirm their spanwise coherence. The control mechanism was related to the formation of these spanwise LCS. The authors argued that pVGJ are able to generate spanwise LCS as a result of the hydrodynamic instability mechanisms of the separated shear layer. Since an inflection point is present in the velocity profile, the flow is susceptible to the Kelvin–Helmholtz (K–H) instability. More recent studies by Marxen et al. (2015), Sato et al. (2015) and Buchmann et al. (2013) also observe spanwise LCS that are created due to the K–H instability mechanism. When steady forcing and pulsed forcing were compared, Postl et al. (2011) found that pulsed blowing is significantly more effective when the same momentum coefficient was used for the actuation.

Despite the improved efficiency of periodic-based active control methods with respect to both steady active and passive control, they have been difficult to apply in practice owing to the complexity of the control devices (Sato et al., 2015). The review paper of Cattafesta and Sheplak (2011) provides many details on the advantages and disadvantages of various actuators. The development of new actuation devices and material systems has enabled novel approaches to periodic flow control to be explored. Munday and Jacob (2002) used a thin, flexible piezoelectric THUNDER actuator, developed at NASA, to morph the surface of an airfoil. When embedded in a surface or attached to flexible structures such actuators provide a distributed force with little power consumption. They are also very light and easy to integrate to the surface of an airfoil, thus enabling their practical use and maximizing the possible aerodynamic gains. Munday and Jacob (2002) performed both static and dynamic morphing tests. While their static tests did not prove very successful, dynamic actuation was found to significantly reduce flow separation. Local wall oscillation in the suction side very close to the leading edge was also considered in the 2D numerical study of Wang et al. (2015). The authors found that when the frequency of oscillation locks into the frequency of the flow, vortices are formed close to the leading edge, they roll along the surface and maintain a low pressure distribution, thereby enhancing lift. The Reynolds number was very low, equal to 5000, and the dominant flow frequency was due to vortex shedding.

The effectiveness of periodic surface morphing of the suction side has been recently demonstrated experimentally for a NACA-4415 airfoil at $Re_c = 50,000$ and various angles of attack (Jones, 2016; Jones et al., 2017). In this paper, we use DNS to investigate this form of actuation for the same airfoil and Reynolds number. Due to the cost of computations, we restrict our simulations to 0° angle of attack. The surface morphing poses additional computational challenges because it necessitates the use of deforming meshes. The central aim is to elucidate further the effect of this form of actuation on the flow characteristics.

The paper is organized as follows. Section 2 presents the computational methodology and discretization details. This is followed by Section 3 with results from the static (i.e. unactuated) airfoil, while Section 4 presents results from 3 actuation frequencies. Finally Section 5 summarizes the main findings of the paper.

2. Computational methodology

2.1. Governing equations and solution details

Due to the variation of the solution domain with time when the airfoil suction side is periodically morphed, the integral form of the incompressible Navier–Stokes and continuity equations is considered (refer to Ferziger and Peric, 2002 for details about their derivation). For an arbitrarily moving and deforming control volume (CV) with bounding surface (S), the equations take the form

$$\frac{d}{dt}\int_{CV}\rho u_i dV + \int_S \rho u_i \left(u_j - u_{p_j}\right) n_j dS = \int_S \left(-p i_i + \tau_{ij} i_j\right) dS \tag{1}$$

$$\frac{d}{dt}\int_{CV} dV + \int_S \left(u_i - u_{p_i}\right) n_i dS = 0 \tag{2}$$

where u_i, u_{p_i} $(i = 1, 2, 3)$ are the velocity components of the fluid and the control volume surface respectively in the Cartesian directions x_i, $\tau_{ij} = \mu(\partial u_i/\partial x_j + \partial u_j/\partial x_i)$ is the viscous stress tensor, i_i is the unit vector in the ith direction, n_j are the components of the unit vector normal to the bounding surface S (pointing outwards), while p, ρ and μ are the pressure, density and dynamic viscosity respectively. For the static (i.e. unactuated) case, $u_{p_i} = 0$. For the actuated case, u_{p_i} is determined from the surface motion as explained later in Section 2.2.

The solution of Eqs. (1) and (2) provides the velocities and pressure at spatial locations that vary with time. The time derivative d/dt refers to the rate of change at two different positions of the control volume. For this reason, we denote the time operator by d/dt, and not by $\partial/\partial t$ that commonly refers to a fixed position in space. The above has implications when computing long time-average quantities (refer to Section 4.3). Due to the periodicity of the actuation, phase-averaged quantities (reported in Section 4.2) are not affected, because the spatial location of the control volume is the same at constant phase.

The finite volume method was used to discretize these equations. In order to avoid the generation of artificial mass sources (or sinks) when the cell faces move relative to each other, the discretization should satisfy the Space Conservation Law (refer to Demirdžić and Perić, 1988; Ferziger and Peric, 2002)

$$\frac{d}{dt}\int_{CV} dV - \int_S u_{p_i} n_i \, dS = 0. \tag{3}$$

This law can be thought of as the continuity equation at vanishing fluid velocity.

The set of Eqs. (1) and (2) was discretized and solved using the OpenFOAM package, version 2.2.2. A second order central scheme was employed for the approximation of the face fluxes and the Crank–Nikolson second order scheme for time advancement. At each time step, an iterative approach is employed that consists of an external and an internal loop. In the internal loop, the PISO algorithm (Issa, 1986) is applied in which the coefficients of the discretized momentum equations are kept constant and the pressure correction equation is solved multiple times (usually 2–3). After each correction, the velocities are updated and the continuity equation is satisfied to a tight tolerance (10^{-6}) before exiting the loop. In the external loop, the coefficients of the momentum equations are calculated using the new velocities and the internal loop is called again. The process is repeated until convergence of the full nonlinear set. This approach is computationally expensive compared to the standard PISO algorithm (in which only the internal loop is called every time step) but proved to be very robust for the present challenging simulations that involve mesh motion.

A C-type grid was generated around the airfoil. The faces of the control volumes form a curvilinear, body-fitted grid with coordinates (ζ, η). The domain boundaries are shown schematically in Fig. 1. The origin of the $x - y$ coordinates is the leading edge of the airfoil. The boundaries in the x–y plane are set to $10c$ away from the airfoil. The size of the domain is determined by the requirement to capture correctly the potential pressure field around the airfoil. For the flow around a NACA-0018 at 10° angle of attack and Reynolds 10^4 Zhang and Samtaney (2015) fixed all boundaries $10c$ away from the airfoil surface. In the DNS study by Jones et al. (2008), for flow past a NACA-0012 airfoil at $Re_c = 5 \times 10^4$ and 5° angle of attack, the boundaries were located at a distance $5.3c$. This modest domain size was found to be sufficient to capture the outer potential flow (computations in a larger domain with radius $7.3C$ showed small variation in the pressure distribution). In the present simulations, the angle of attack is 0°, so the lateral extent of pressure disturbance due to the presence of the airfoil is limited. A domain size of $10c$ is considered therefore sufficient.

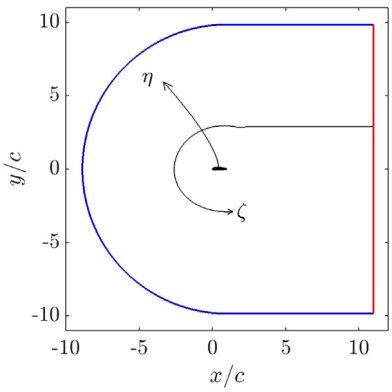

Fig. 1. C-type computational domain based on curvilinear coordinates η and ζ.

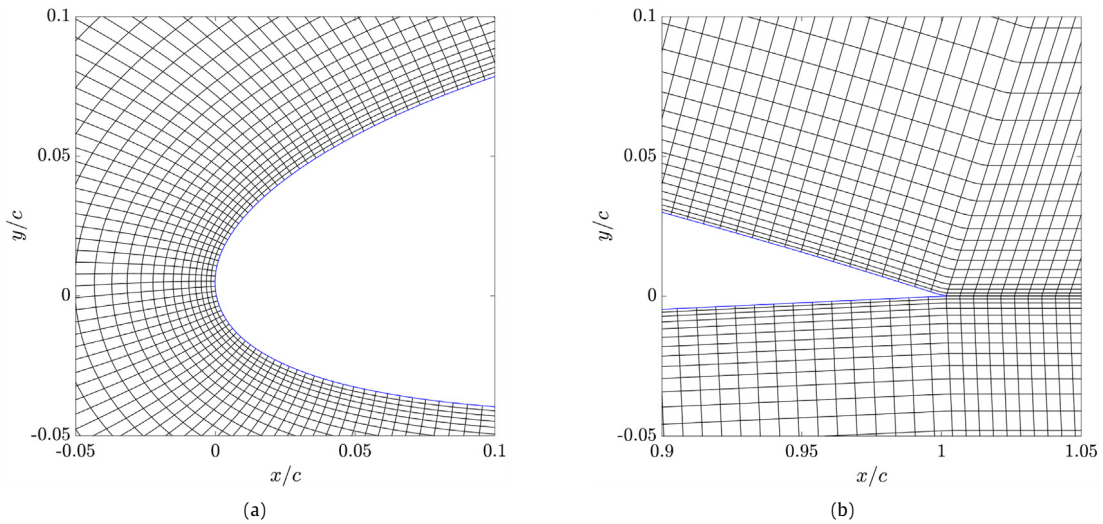

Fig. 2. Grid lines in the near wall region after orthogonality was enforced by elliptic refinement and Neumann boundary condition at the wall (a) leading edge; (b) trailing edge. Only every 4th line is plotted for figure clarity.

The grid boundary node distribution is specified on the airfoil surface and the outer boundary. In total 1024 points were specified in the ζ direction around the airfoil surface, 220 in the η direction and 1084 in the wake. The domain was extruded 0.2c in the z direction to form a 3D grid. This has been found to be sufficient for capturing the 3D flow behavior in previous studies (Jones et al., 2008; Brehm et al., 2013). A coarse grid with 16 planes in the z direction is used to initialize the simulations. A finer grid, with 64 planes in the z direction, is then employed for better resolution. The total number of cells for the fine grid is 45 million.

The internal mesh is generated using linear transfinite interpolation between the corresponding boundary coordinates on the airfoil and the outer boundary (Rhodes and Santer, 2012). An elliptic refinement with a Neumann boundary condition is implemented to increase grid orthogonality at the airfoil surface and improve accuracy in the near-wall region. The resulting near-wall grid lines in the vicinity of the leading and trailing edges can be seen in Fig. 2. Using the elliptic-Neumann refinement technique the maximum non-orthogonality is reduced from 73° to 26°, and the mean from 19° to 6°.

A pressure outlet was used at the outflow exit (shown as red line in Fig. 1) and a uniform free stream velocity was used on the rest of the external boundary (shown as blue curve in Fig. 1). The no-slip condition was enforced on the airfoil surface. A time-step, $\Delta t = 1 \times 10^{-4}$ was used to keep to maximum CFL number below 1.

The simulation was started from uniform initial conditions (free stream velocity). After the flow developed fully in the coarse mesh (at $t^* = tU_\infty/c = 20$), the instantaneous velocity and pressure fields were interpolated to the fine grid and used as initial conditions. The simulation was then run until a statistical steady-state was achieved. For the unactuated airfoil, C_D reaches statistical convergence when $t^* = 7.7$ but C_L takes until $t^* = 12.3$ to converge. The solution at $t^* = 16$ was considered to be fully developed. The simulation was then restarted from $t^* = 16$ and run until $t^* = 20$. Details about the statistical convergence of the results for the morphing airfoil simulations are provided in Section 4.

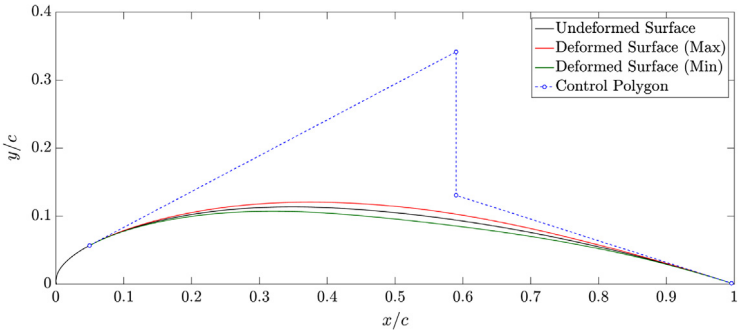

Fig. 3. A Bézier control polygon defining deformed surface coordinates with C^1 continuity. The peak-to-peak displacement is multiplied by a factor of 5 for clarity.

The time-average friction velocity, u^*, was used to obtain the x^+, y^+ and z^+ values at the centroids of the cells closest to the wall. The maximum y^+ and z^+ values are 1.5 and 18.9 respectively and occur close to the leading edge. The flow at this location is still laminar and the friction velocity, u^*, is maximum owing to the large acceleration of the flow around the leading edge. Further downstream, the maximum y^+ drops to 0.55 and the maximum z^+ to 8.5. The maximum x^+ value is 8.3. These values are similar to those reported in other recent DNS studies involving laminar separation on airfoils (for example Zhang and Samtaney (2015) report 5, 0.6, 5 for x^+, y^+ and z^+ respectively while Jones et al. (2008) 3.4, 1.0 and 6.5 for the same parameters). In total 10 cells are used to discretize the near wall region with $y^+ = [0 - 10]$ (in Jones et al., 2008 9 points were placed in the same region).

2.2. Implementation of periodic surface morphing

In the experimental investigation of surface morphing (Jones, 2016; Jones et al., 2017), the flow was found to have little effect on the surface motion, thereby in the simulations it was not deemed necessary to solve a coupled fluid-structure interaction problem. The amplitude distribution and the angular frequency define completely the motion of the moving boundary. In the physical model, the leading and trailing edges of the deforming portion of the surface – herein referred to as the control surface – are attached to the airfoil body by a rigid bond and a slide joint respectively. As a result, the wall-normal displacement of the control surface is zero at these locations ($x/c = 0.07$ and 0.93) and varies smoothly in-between. To ensure that the surface motion in the computational model is physically realistic, a Bézier curve was used to define a C^1 continuous function from which the amplitude distribution was obtained. A Bézier curve is a parametric curve which is defined by the locations of 4 control points, 2 of which lie at each end of the curve, as seen in Fig. 3.

The Bézier curve was discretized and the coordinates of the intersection point between the curve and the vector normal to every cell face of the undeformed surface were computed (refer to Fig. 4(a)). The distance between the undeformed wall-face center and the corresponding point on the Bézier curve is the amplitude of that particular wall-face. The amplitude distribution along the chord, $A(x)$, can be seen in Fig. 4(b). The value is zero at $x/c = 0.07$ and 0.93 as required, and varies smoothly along the surface, with a peak-to-peak displacement of about 0.2% at $x/c = 0.4$, matching the conditions of the experiments. The frequency with which that surface moves is given by

$$\eta(x, t) = A(x) \sin(2\pi V_{f+} t^*) \tag{4}$$

where $\eta(x, t)$ is the local displacement in the direction normal to the undeformed surface and V_{f+} is the actuation frequency, non-dimensionalized by chord length, c, and freestream velocity, U_∞.

The temporal variation of the coordinates of the internal grid points is now considered. The purpose of the internal grid point motion is to accommodate the prescribed boundary motion as defined above, whilst preserving grid quality. Recall that the grid velocity u_{p_i} appears in the equations of motion (1) and (2). On the airfoil boundary u_{p_i} is equal to the prescribed velocity and at the external boundaries is equal to zero. A spatial distribution of u_{p_i} is therefore sought that provides acceptable grid distortion at each time instant. A smooth distribution is obtained if the grid velocities satisfy the Laplace equation, with a variable diffusion coefficient set equal to the square of the inverse of the distance from the moving surface, l, i.e.

$$\frac{\partial}{\partial x_j}\left(\frac{1}{l^2}\frac{\partial u_{p_i}}{\partial x_j}\right) = 0. \tag{5}$$

The prescribed motion of the domain boundaries acts as a Dirichlet boundary condition for this equation.

The solution of (5) is computed iteratively prior to the external iterative loop at each time-step. The Laplacian operator ensures that the displacement of the internal grid points is diffused smoothly inside the domain, as can be seen in Fig. 5(a). The grid quality in the near wall region must be maintained, so as little cell distortion as possible is desirable. As can be seen from Fig. 5(b), the maximum non-orthogonality is unaffected by the grid motion and the mean non-orthogonality varies by less than 0.2% throughout the actuation cycle.

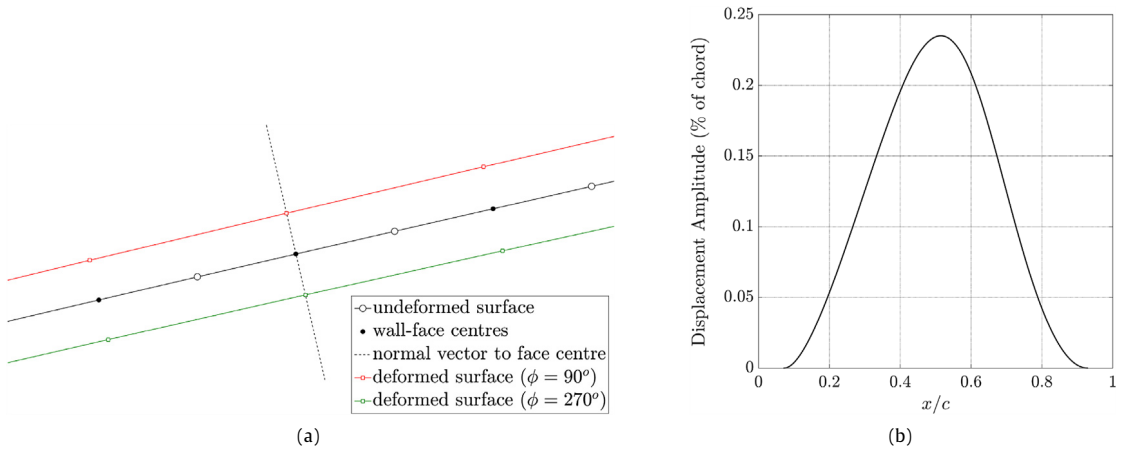

Fig. 4. Definition of the external boundary motion: (a) Determination of amplitude as distance between points located along the normal to the cell face in the undeformed configuration; (b) Distribution of peak-to-peak amplitude along chord.

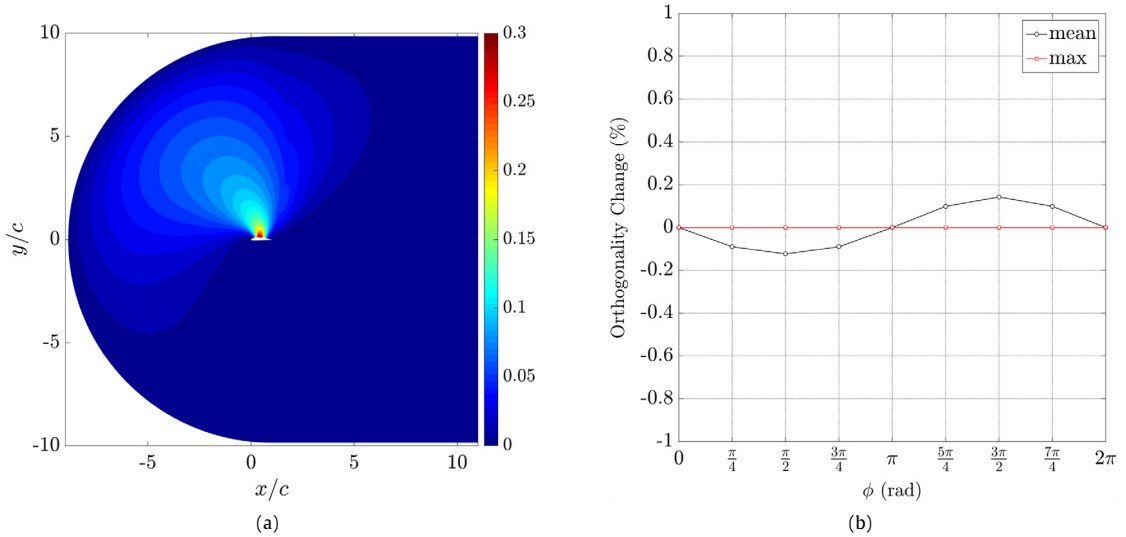

Fig. 5. (a) Diffusion of the internal grid point motion inside the domain. Contours show the cell centroid displacement as percentage of the chord, (b) Change of grid orthogonality during one actuation cycle.

3. Results from static airfoil simulations

In this section the flow field around the static (i.e. unactuated) airfoil is characterized. Time-average results are first discussed, followed by analysis of the dominant flow structures obtained using the Dynamic Mode Decomposition (DMD) method (Schmid, 2010; Jovanovic et al., 2014). In all cases examined in this paper, the flow is homogeneous in the spanwise direction, and the results are also spanwise-averaged to increase the sample size and improve convergence of statistics. When the flow is inhomogeneous in this direction (as in Wahidi et al. (2014) due to spanwise periodic cambering, or in Gordnier et al. (2013) due to spanwise flexibility) only time-averaging can be performed.

3.1. Time-average results

Fig. 6(a) shows the average spanwise vorticity. The initially attached sheet of strong vorticity, $\overline{\Omega_z}$, separates from the airfoil surface at $x/c = 0.42$ and remains concentrated exclusively in a thin separated shear layer until $x/c \approx 0.85$. Further downstream, the magnitude of $\overline{\Omega_z}$ decreases and the region of high vorticity becomes more dispersed. This dispersion is the result of turbulent transition. This can be confirmed from inspection of Fig. 6(b) in which contours of turbulent kinetic energy, referred to as TKE below, are superimposed on velocity vectors in the area around the trailing edge.

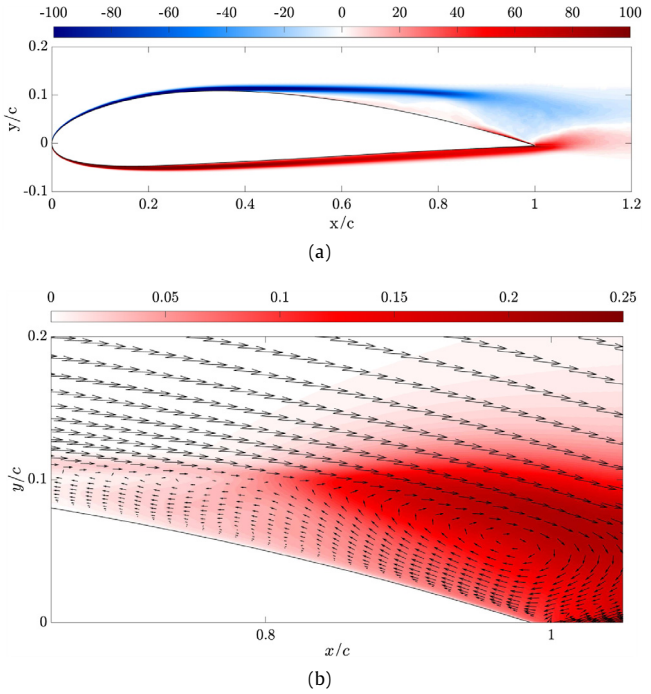

Fig. 6. Iso-contours of time and spanwise averaged flow fields (a) $\overline{\Omega_z}$; (b) TKE contours superimposed on local velocity vectors showing a reverse flow region.

Upstream of $x/c = 0.8$ the levels of TKE are small, but downstream TKE increases rapidly, indicating turbulent transition. Horton (1969) found that a reverse-flow vortex and pressure recovery accompany the turbulent portion of a laminar separation bubble. Fig. 6(b) shows that indeed a strong reverse flow vortex is confined to a region of high TKE. Moreover, a quiescent flow is expected to develop beneath the laminar portion of the shear layer (Tani, 1964). Fig. 6(b) indicates that the time-averaged velocity magnitude in the region underneath the strong concentrated shear layer is indeed very close to zero.

The quiescent flow also results in a flattened region in the surface pressure distribution, known as a pressure plateau (Yarusevych et al., 2009). In Fig. 7 a pressure plateau is found to extend from a location shortly downstream of separation to a point close to the trailing edge. A small pressure recovery occurs in the aft 5% of the airfoil as a result of transition. Since the flow transitions close to the trailing edge, turbulent reattachment does not occur at the surface of the airfoil and the pressure recovery is weak. Instead, an open recirculation zone is formed that extends to the near wake, as seen in Fig. 6(b). The presence of recirculation leads to poor aerodynamic performance; more details and comparison with the performance of morphing airfoil are presented in Section 4.4.

Inspection of Fig. 4(b) reveals that the maximum amplitude of deformation is located slightly downstream of the separation point. From research on separation control using synthetic jets, it is known that the optimal location of actuation is upstream of separation. In the present case, the morphing profile was selected to match the experimental actuation as closely as possible. As can be seen from Fig. 4(b) there is significant actuation amplitude from the start of morphing (at $x/c = 0.07$) to the point of separation ($x/c = 0.42$). As will be seen in Section 4, this has beneficial effect on the airfoil characteristics.

The flow development can be summarized as laminar separation with transition but without reattachment. This is exactly the type of flow observed also experimentally (Jones, 2016; Jones et al., 2017). There is also good quantitative matching between experiments and simulations. Velocity profiles at 3 locations in the airfoil wake are shown in Fig. 8. These are compared with the experimental profiles (two of the profiles were obtained using hotwire and one with PIV). At $x/c = 1.1$ experiments and simulations are in reasonably good agreement. Further downstream, there is an 8% difference between the maximum velocity deficit. Differences can be attributed to the following reasons: first, the computations do not account for the incoming turbulence intensity at the inlet, and secondly the tunnel had fixed walls at $\pm 2c$ in the cross-stream (i.e. y direction), while in the computations a constant velocity U_∞ was imposed as boundary condition at $10c$.

3.2. Dominant structures in the separating shear layer

In order to understand the nature of the structures that govern the dynamics of the shear layer in the uncontrolled flow field, DMD (Schmid, 2010; Jovanovic et al., 2014) was employed. The method provides the most dynamically important

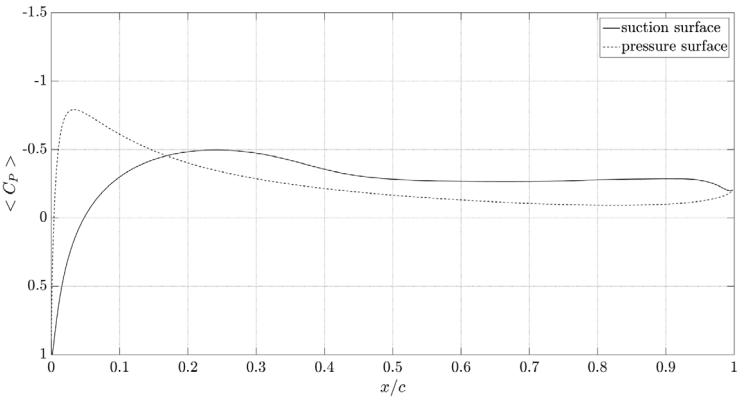

Fig. 7. Time-averaged distribution of C_P.

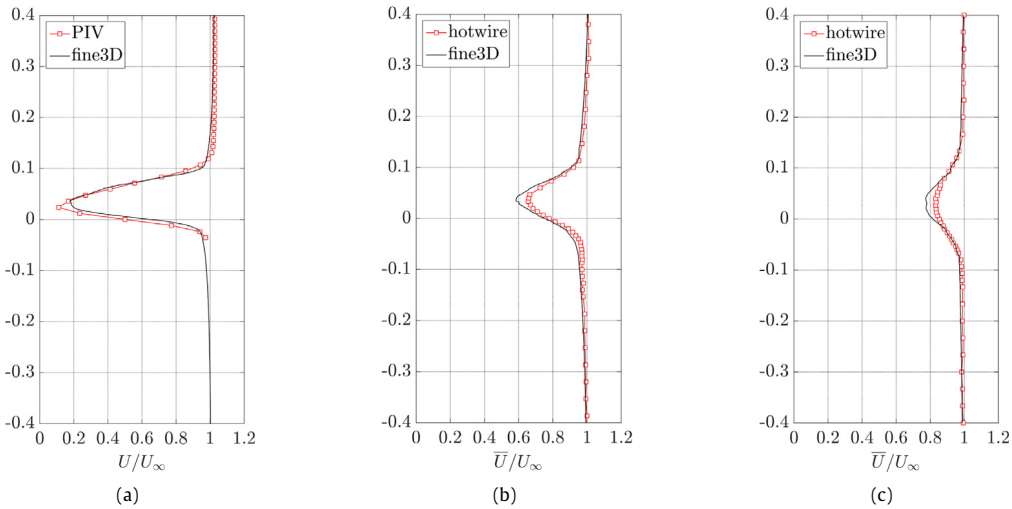

Fig. 8. Comparison of wake profiles at: (a) $x/c = 1.10$; (b) $x/c = 1.25$; (c) $x/c = 1.50$.

structures, their spatial distribution and their frequency. For a thorough description of the method the reader is referred to Schmid (2010), Jovanovic et al. (2014) and Tu et al. (2014).

Snapshots of the 3D instantaneous flow field are captured every 125 time-steps, i.e. 321 snapshots were captured during a time period of $\Delta T^* = 4$ after the flow has fully developed. We perform DMD, using the algorithm described in Jovanovic et al. (2014), focusing on a $x - y$ region $[0.7 : 1.0] \times [0 : 0.2]$, where the separating and transitioning shear layer is located. Fig. 9(a) shows the spectrum of the DMD modes, which exhibits a clear peak at $St_c \equiv fc/U_\infty = 4.9$. This figure is in very close agreement with the experimental value of 4.8 (corresponding to 170 Hz) obtained from the spectra of the cross-stream velocity component (Jones, 2016; Jones et al., 2017). This matching provides further evidence of the validity of the simulations. Study of the energy content in this region of the flow field reveals that the time-average flow makes the single largest contribution (as expected), while the dominant shear layer mode contributes 7% of the total energy.

Fig. 9(b) shows the spanwise-averaged contours of the cross-stream velocity of the dominant mode. It is evident that this mode represents the Kelvin–Helmholtz instability that is known to develop in separating shear layers (Dovgal et al., 1994; Ho and Huerre, 1984; Marxen et al., 2013; Kotapati et al., 2010). The structures are well defined and are seen to persist inside the area of transition. Due to spanwise averaging, they also appear smooth. The full three-dimensional spatial structure of the dominant mode is shown in Fig. 9(c). The structures are still evident but they appear more corrugated due to the action of background turbulence.

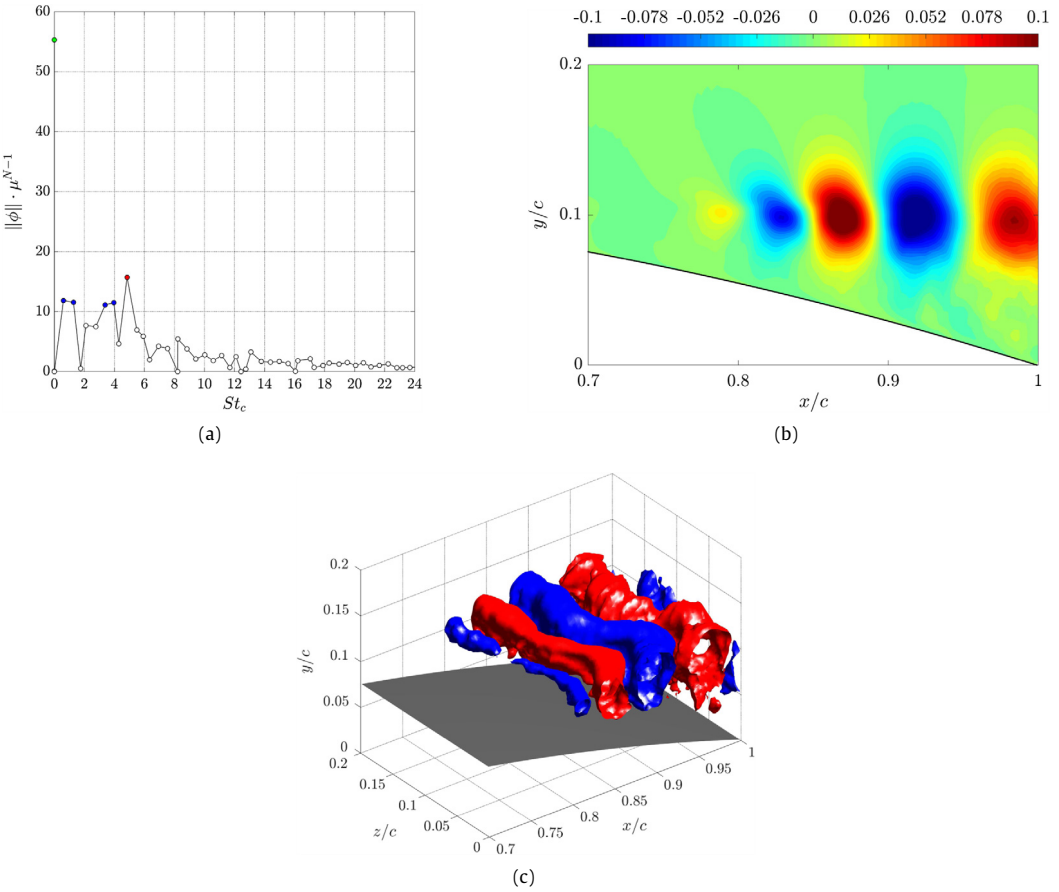

Fig. 9. Spectral analysis of the trailing edge using DMD: (a) Frequency Spectrum; (b) Spanwise-averaged dominant DMD mode (cross-stream velocity contours). (c) Iso-surfaces of the cross-stream velocity component of the dominant DMD mode.

4. Results from morphing airfoil simulations

In this section, the instantaneous, phase-averaged and time-averaged flow fields are analyzed in order to provide insight into the flow control mechanism of surface morphing. As mentioned in Section 2.2, the actuation frequencies, V_f, are non-dimensionalized as

$$V_{f^+} = \frac{V_f c}{U_\infty} \tag{6}$$

to give the reduced frequencies, V_{f^+}. Three frequencies were chosen for in-depth investigation $V_{f^+} = 0.4$, 2 and 5, which correspond to $V_f = 14$, 71 and 177 Hz respectively in the actual experiment (Jones, 2016; Jones et al., 2017). The higher frequency was chosen to be close to the shear layer frequency identified in the previous section. Due to structural constraints, this frequency could not be tested experimentally with the current set up. For each V_{f^+} tested, the solution at the final time instant of the static simulations (i.e. $t^* = 20$) was used as initial condition. The flow was then allowed to develop for each V_{f^+} from the same starting conditions. The surface morphing assumes the form given by Eq. (4) in Section 2.2. The argument $\phi = 2\pi V_{f^+} t^*$ in Eq. (6) is called the phase of the actuation below. Note that because the deformation is fixed, the amplitude of the actuation velocity is proportional to the frequency V_{f^+}.

4.1. Instantaneous response of the flow field to surface motion

Fig. 10 compares the space–time plots of the instantaneous spanwise-averaged friction coefficient, C_f, for the three frequencies in a time interval of 5 time units since the start of actuation. This corresponds to 3, 10 and 25 actuation cycles for $V_{f^+} = 0.4$, 2 and 5 respectively. For all cases, the strong positive C_f from $0 < x/c < 0.4$ is a consequence of the attached flow accelerating around the airfoil's leading edge. Further downstream, C_f becomes zero at the point of separation and is followed by a region of weak negative C_f. This is a result of the slowly recirculating flow in the dead-air region below

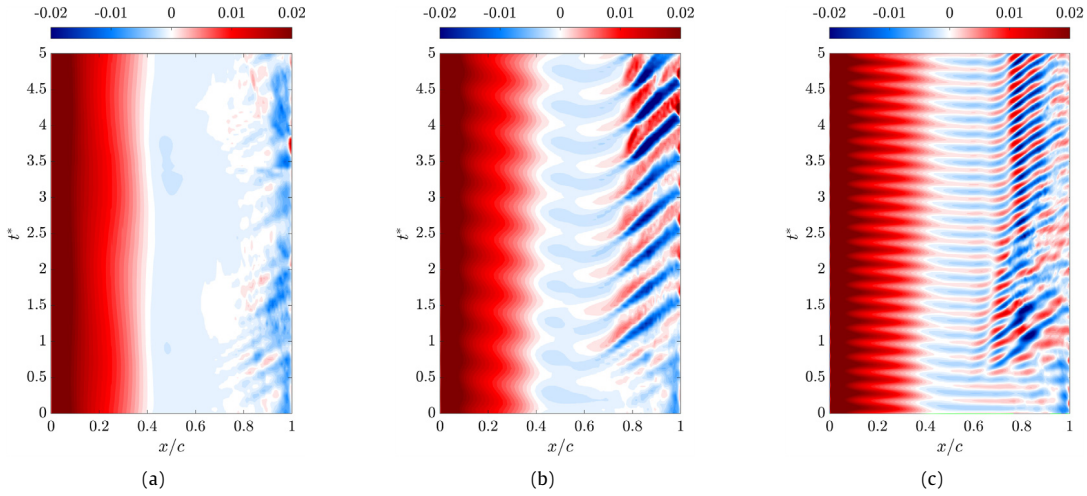

Fig. 10. Space–time diagram of instantaneous spanwise-averaged C_f: (a) $V_{f+} = 0.4$; (b) $V_{f+} = 2$; (c) $V_{f+} = 5$. Time $t^* = 0$ indicates start of actuation.

the laminar portion of the separated shear layer (similar to that described in Section 3.1 for the unactuated case). When $V_{f+} = 0.4$, the slowly recirculating region extends all the way to $x/c = 0.9$ before a small region of stronger negative C_f occurs, confined to $0.9 < x/c < 1.0$. This is due to the stronger recirculation region forming underneath the transitioning shear layer, again very similar to the unactuated case. Clearly the flow field for the lowest frequency has many similarities to the flow around the static airfoil, at least in terms of C_f distribution.

In contrast, substantial changes in the distribution of C_f downstream of separation take place when $V_{f+} = 2$ and 5. The slowly recirculating region is still present downstream of separation but terminates at $x/c \approx 0.7$ and an alternating positive and negative distribution is set up. The appearance of regions of strong negative C_f is indicative of shear stress resulting from clockwise rotating vortices convecting downstream. The regions of strong positive C_f are located between two adjacent vortices, an area known as a 'braid' region (Marxen et al., 2013).

In both $V_{f+} = 2$ (Fig. 10(b)) and $V_{f+} = 5$ (Fig. 10(c)), the first strong negative C_f occurs at $t^* \approx 0.8$. Clearly the flow needs some time to respond to actuation. When $V_{f+} = 2$, the regions are thicker and fewer than when $V_{f+} = 5$, because the actuation period is longer. Closer inspection of Fig. 10 reveals that there is slow variation of C_f from one actuation cycle to the next, in other words the flow has not yet reached a repeatable periodic state in the time interval examined.

Insight into the variation of the C_f distributions is given by the instantaneous, spanwise-averaged Ω_z contours shown in Fig. 11. Fig. 11(a) depicts the vorticity exactly at the instant of actuation start (i.e. $\phi = 0°$ of the first actuation cycle) and is therefore the same for all values of V_{f+}. The figures beneath correspond to the same phase of actuation (i.e. $\phi = 0°$) for the first 4 cycles of each actuation frequency. When $V_{f+} = 0.4$, the shear layer can be seen to roll up and form a clockwise-rotating vortex at $x/c \approx 0.9$. This vortex remains at the same location and the same distance away from the airfoil surface from one cycle to the next. The negative values of C_f in the region $0.9 < x/c < 1.0$ seen in Fig. 10(a) are explained by the presence of this rolled-up shear layer vortex, rotating in the clockwise direction. The relatively weak magnitude of C_f is a result of the vortex remaining far from the airfoil surface.

The roll-up of the separated shear layer is also observed at the beginning of the 3rd and 5th cycles when $V_{f+} = 2$ and 5 respectively. However, compared to $V_{f+} = 0.4$, this occurs much further upstream and causes a significant change in the flow development. This explains why the region of slowly recirculating fluid only extends up to $x/c \approx 0.7$ at these two frequencies, as shown in Fig. 10(b) and (c). The vortices at the two higher frequencies also appear more distinct and are located closer to the surface than when $V_{f+} = 0.4$, causing the higher negative C_f values.

To investigate further the onset of the roll-up process, 7 instantaneous snapshots of the spanwise-averaged Ω_z are shown in Figs. 12 and 13 for $V_{f+} = 2$ and 5 respectively. The cycles shown are the 3rd and 5th for the two frequencies respectively (these are the cycles in which shear layer roll-up first occurs). The snapshots begin from $\phi = 45°$ (top). Each subsequent figure from top to bottom is 45° apart from the previous one. When the corresponding $\phi = 0°$ snapshot from Fig. 11 is included, the entire actuation cycle in which shear layer roll-up first occurs is presented.

For $V_{f+} = 2$, Fig. 12, a waviness is present at $x/c = 0.8$. As the actuation cycle progresses, this waviness is amplified until it develops into a distinct vortex that is shed into to the wake and another vortex develops behind it, at roughly $x/c = 0.75$. This also sheds before a further vortex forms, even further upstream, at $x/c = 0.7$ ($\phi = 315°$). A similar pattern is observed when $V_{f+} = 5$ but the initial waviness contains two vortices. As the cycle progresses, these vortices become much more clear and distinct.

It is clear from the difference between the $V_{f+} = 0.4$ case and the $V_{f+} = 2$ and 5 cases in Fig. 10 that the amplification of the K–H instability has a profound impact on the downstream development of the flow field and results in earlier roll-up

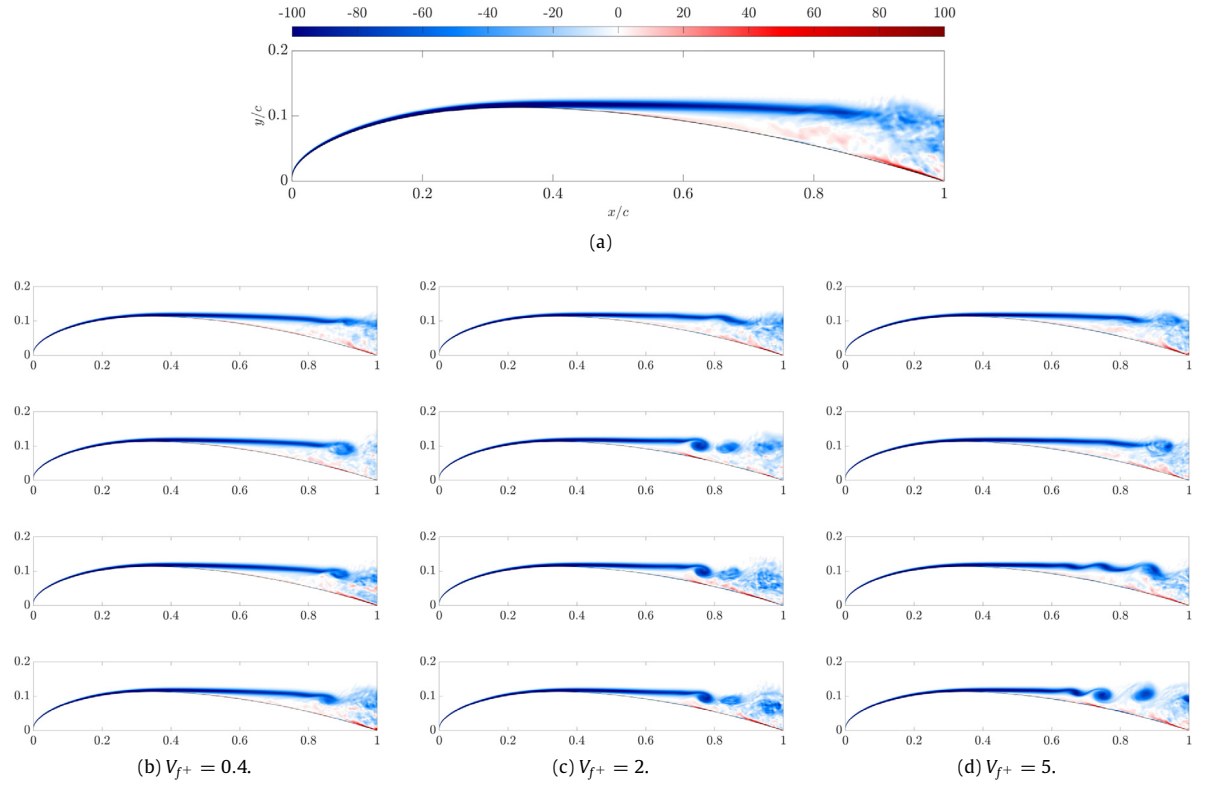

Fig. 11. Iso-contours of instantaneous spanwise-averaged Ω_z at the beginning of the first 5 actuation cycles (i.e. $\phi = 0°$ for all figures). Cycle number increases from top to bottom: (a) $\phi = 0°$ of first cycle (instance of actuation start is the same for all V_{f^+}).

of the shear layer. As will be seen later, this change in flow development plays a vital role in improving the aerodynamic performance of the airfoil.

To investigate the structure of these vortices, Fig. 14 displays instantaneous snapshots of the streamwise velocity, u/U_∞, and an isosurface of Q-criterion at $\phi = 360°$ for the 2nd and 4th cycles for $V_{f^+} = 2$ and 5 respectively. This time instant corresponds to the end of the actuation cycle in which shear layer roll-up first occurred, and it is equivalent to $\phi = 0°$ for 3rd and 5th cycle in Fig. 11. Q is defined as $Q = \frac{1}{2}(u^2_{i,i} - u_{i,j}u_{j,i}) = \frac{1}{2}(\|\mathbf{\Omega}\|^2 - \|\mathbf{S}\|^2)$, where $\mathbf{\Omega}$ and $\mathbf{S}$ are the rotation and strain rate tensors respectively. When $Q > 0$ the rotation rate dominates the strain rate, and serves to identify a vortex core. In Fig. 14, the Q-criterion reveals the appearance of large, spanwise-coherent vortical structures (LCS). These LCS are a characteristic feature of the K–H type instability (Marxen et al., 2013). One such structure is seen at $x/c = 0.75$ for ${V_f}^+ = 2$, while 2 structures appear in $x/c = 0.65 - 0.75$ for ${V_f}^+ = 5$. As they propagate downstream the structures lose their spanwise coherence, break down and they entrain high momentum fluid from the outer flow towards the airfoil surface, thus re-energizing the near-wall flow.

As seen for the top plots of Fig. 14, the flow fields still exhibit large regions of separated flow. As can be seen in Fig. 15, this remains true even 4 cycles after the shear layer roll-up first occurred, when the LCS have had the time to propagate beyond the trailing edge and therefore impact upon the entire separated region. Notice however, that the separated regions are suppressed in Fig. 15 compared to Fig. 14 and so the actuation is having a positive effect as the number of actuation cycles increases.

To investigate further the continued development of the flow field under the influence of control, the $V_{f^+} = 2$ simulation was continued until $t^* = 32.5$ so it had also performed 25 cycles — equal to that of $V_{f^+} = 5$ case. The iso-contours of Ω_z, u/U_∞ and the iso-surfaces of $Q = 250$ for $\phi = 360°$ at the end of the 25th cycle are shown in Fig. 16. Comparing the size of the separated regions in Fig. 16 with those in Fig. 14 it is clear the actuation at $V_{f^+} = 2$ and 5 have significantly reduced the size of the separated region. When $V_{f^+} = 5$ the flow appears more spanwise coherent than when $V_{f^+} = 2$ and two LCS are present of the airfoil surface. The enhanced mixing that these produce has almost entirely eliminated the separated region at the trailing edge. Note also how close the separating shear layer is to the airfoil (compare for example Ω_z in Fig. 16(b) and the plots in Fig. 13).

To summarize, the control mechanism began with the early roll-up of the separated shear layer due to the amplification of the K–H instability. This first occurred during the 2nd and 4th cycle for the $V_{f^+} = 2$ and 5 respectively and resulted in the formation of LCS, which are effective at transferring momentum across the boundary layer. The presence of these structures

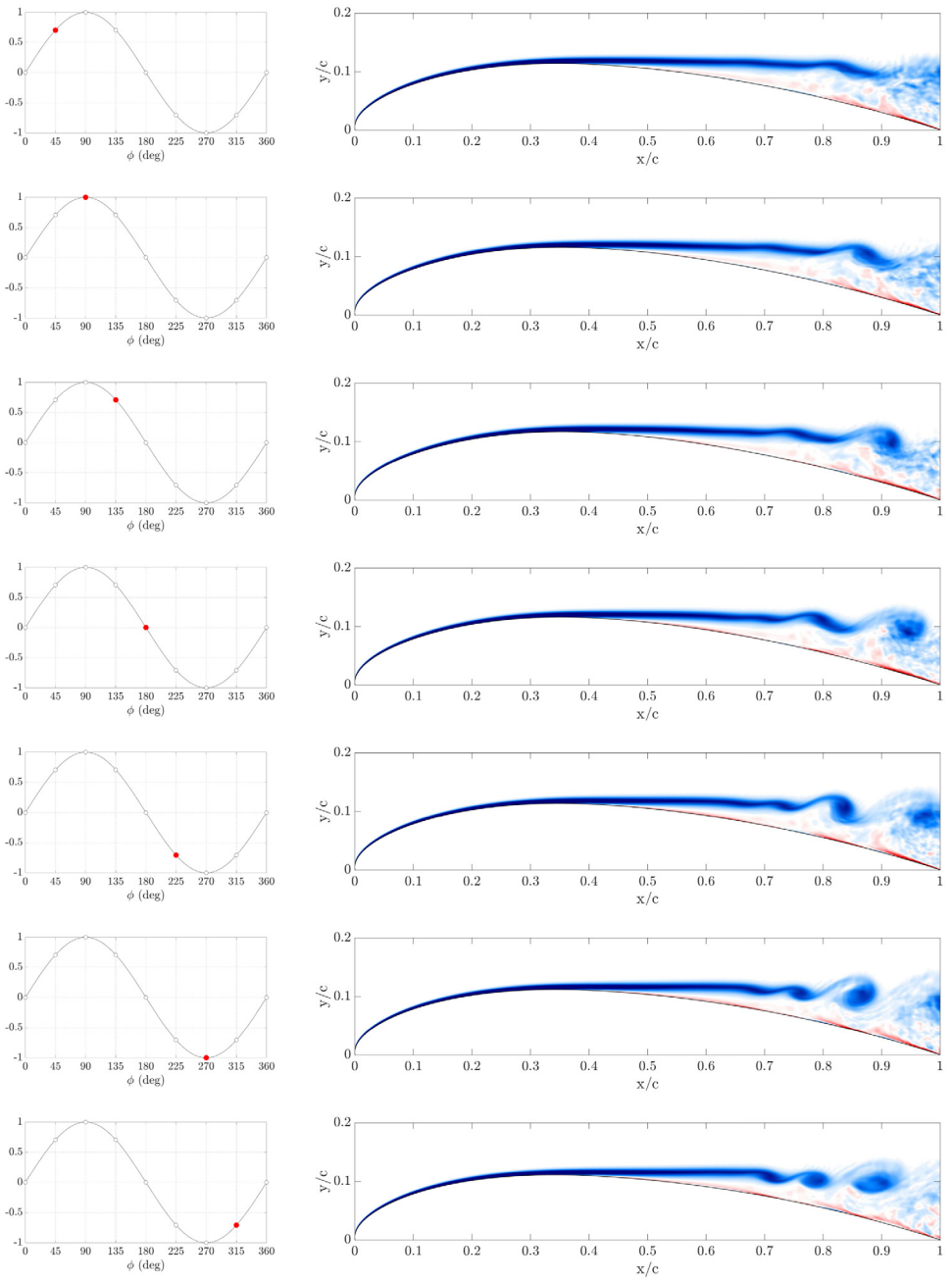

Fig. 12. Contours of instantaneous spanwise-averaged Ω_z depicting the onset of shear layer roll up during the 2nd actuation cycle when $V_{f+} = 2$. Phase angle ϕ increases by 45° from 45° to 315° from top to bottom.

further upstream means more momentum transfer can occur over a larger portion of the airfoil surface. Over time, this has enabled a significant reduction in separation by re-energizing the near-wall flow, helping it to overcome the adverse pressure gradient. From analysis of the flow fields in Figs. 14–16, it has been found that this is a gradual process. As the number of actuation cycles increases, the shear layer gradually gets closer to the airfoil surface and the size of the separated region decreases.

Fig. 17 shows the space–time $x - t^*$ diagram of the spanwise-averaged C_f for the final 10 cycles (i.e. cycles 15–25), which demonstrates that the flow has developed into a periodic pattern after 15 cycles. From the slope of the patterns, one can calculate the convection speed of the structures, and obtain for $V_{f+} = 2$, $U_c = 0.39$; $V_{f+} = 5$, $U_c = 0.43$. The next section will focus on the analysis of the phase-averaged flow.

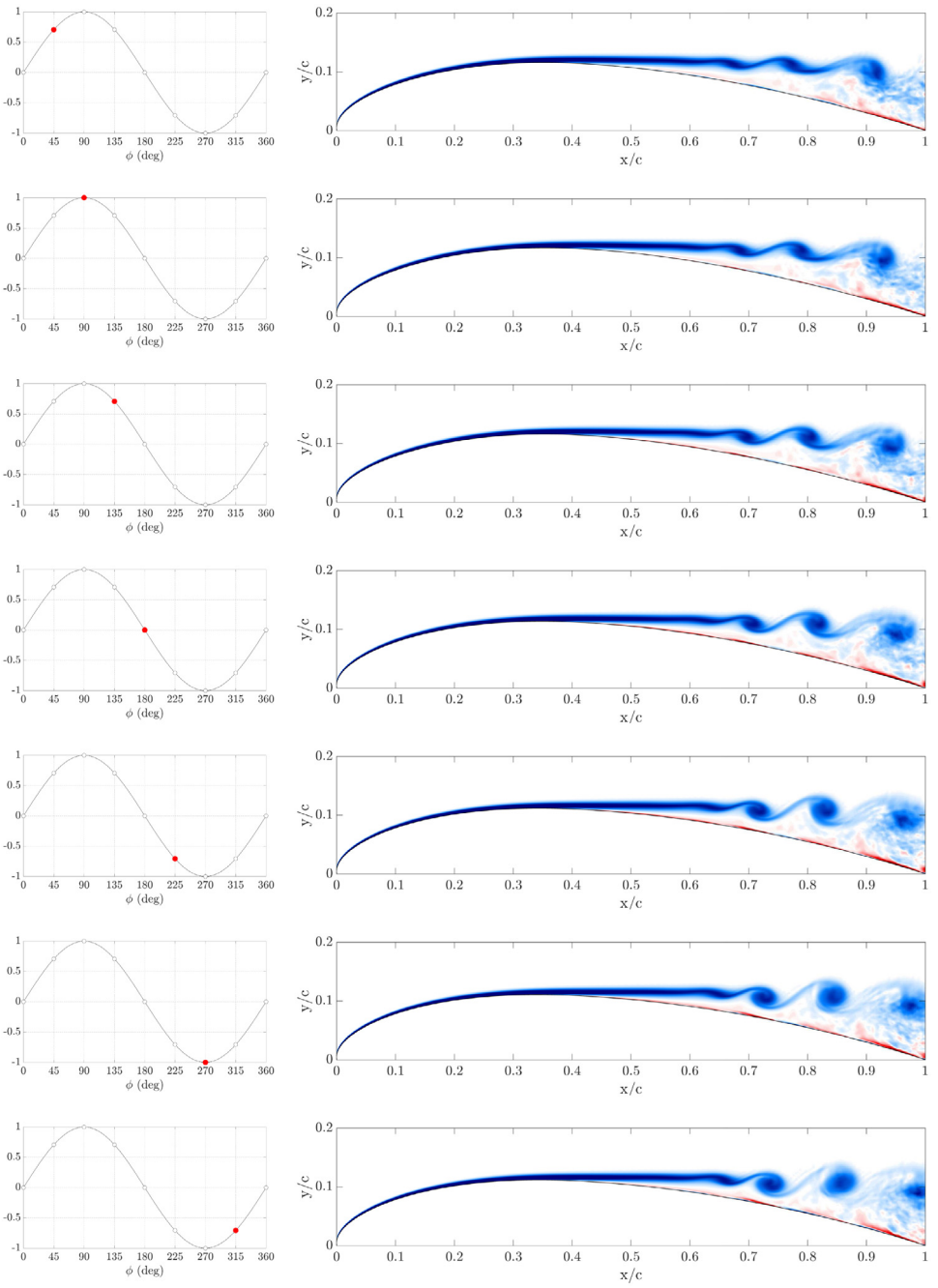

Fig. 13. Contours of instantaneous spanwise-averaged Ω_z depicting the onset of shear layer roll up during the 4th actuation cycle when $V_{f^+} = 5$. Phase angle ϕ increases by 45° from 45° to 315° from top to bottom.

4.2. Phase-averaged results

For a better understanding of the control mechanism, the spanwise-averaged Ω_z and Q-criterion were phase-averaged every 45° for the last 10 cycles. The temporal evolution of the flow fields is shown in Figs. 18 and 19 for one complete cycle for $V_{f^+} = 2$ and 5 respectively.

For $V_{f^+} = 2$, the shear layer at the beginning of the cycle (Fig. 18, $\phi = 0°$) is located much closer to the surface than it was in Fig. 11(a), which is consistent with the large reduction in the size of the separation region observed in Fig. 16. The Q-criterion reveals an LCS located at $x/c \approx 0.8$. As the cycle continues to evolve, the LCS is ejected from the shear layer

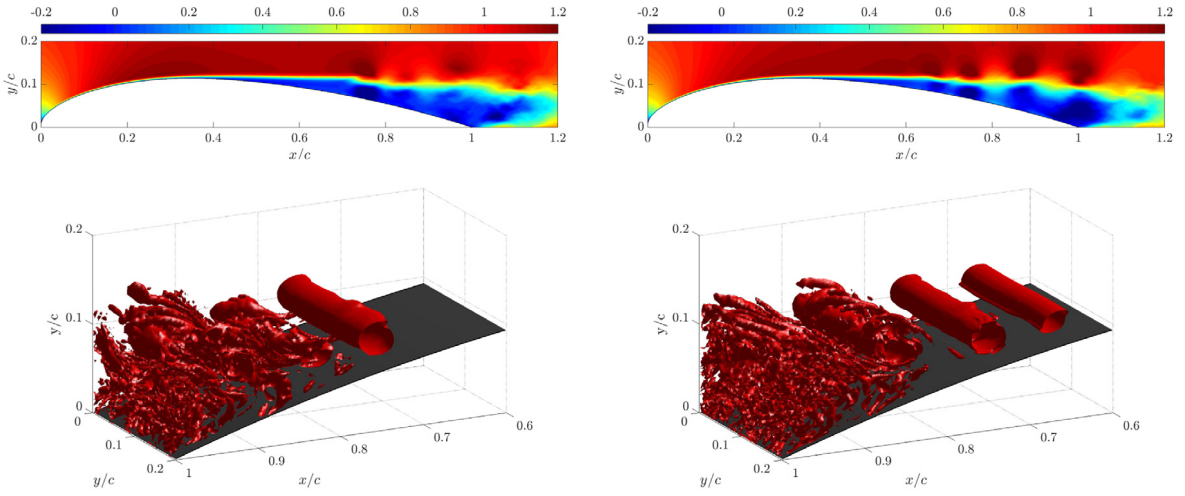

(a) $V_{f+} = 2$ (cycle 2: $\phi = 360°$). (b) $V_{f+} = 5$ (cycle 4: $\phi = 360°$).

Fig. 14. Instantaneous spanwise-averaged u/U_∞ (top) and Q-criterion (bottom) at the end of the cycle ($\phi = 360°$) in which shear layer roll-up first occurred.

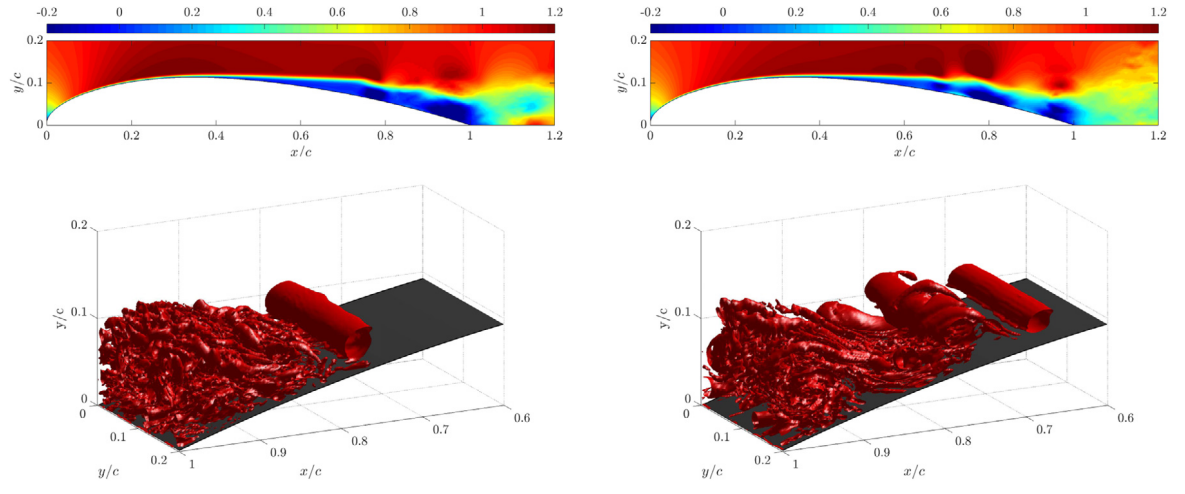

(a) $V_{f+} = 2$ (cycle 6: $\phi = 360°$). (b) $V_{f+} = 5$ (cycle 8: $\phi = 360°$).

Fig. 15. Instantaneous spanwise-averaged u/U_∞ (top) and Q-criterion (bottom) for $\phi = 360°$ 4 cycles after the initial shear layer roll-up occurred.

and propagates towards the trailing edge, losing its spanwise coherence as it does so. By $\phi = 270°$ – the trough in surface motion – the coherence is entirely lost. At $\phi = 315°$, when the surface is moving in an upward direction, a new LCS has been produced at $x/c \approx 0.8$. Note how the coherence of the vortex is related to the motion of the surface. Using the convection speed of $U_c = 0.39$ computed at the end of the previous section, it can be easily computed that within one cycle the vortex has propagated to the trailing edge, therefore it is not surprising to see only one vortex at the suction side.

The above description supports the idea that periodic actuation promotes and regulates the production of LCS (Wygnanski and Newman, 1964). The stronger coherence appears when the phase angle ϕ is in the region $[0°, 90°]$ i.e. when the surface is moving outwards from the average position. Dynamic surface actuation at $V_{f+} = 2$ generates one LCS during the up-stroke of the cycle before ejecting this structure from the shear layer on the down-stroke.

When $V_{f+} = 5$ the shear layer can be seen again to roll up to form an LCS (refer to Fig. 19). The LCS are produced further upstream compared to the $V_{f+} = 2$ case (at $x/c \approx 0.75$) and appear capable of maintaining their spanwise coherence for the duration of the cycle (but of course the period is 2.5 times smaller). Once they propagate beyond $x/c \approx 0.9$ they lose their coherence. The effect can be detected in the C_f coefficient that becomes more chaotic for $x/c > 0.9$ (refer to Fig. 17(b)). It can also been seen that two such structures are present on the airfoil surface, compared to only one for $V_{f+} = 2$. Using

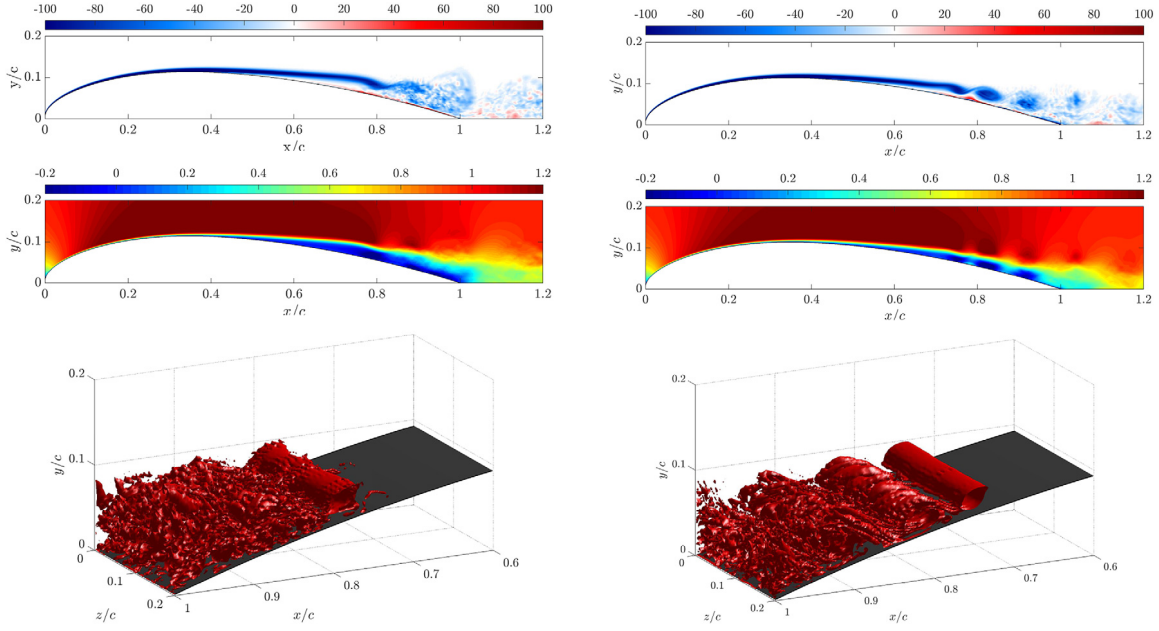

(a) $V_{f^+} = 2$ (cycle 25: $\phi = 360°$). (b) $V_{f^+} = 5$ (cycle 25: $\phi = 360°$).

Fig. 16. Instantaneous spanwise-averaged Ω_z (top), spanwise-averaged u/U_∞ (middle) and Q-criterion (bottom) for $\phi = 360°$ 25 cycles after actuation start.

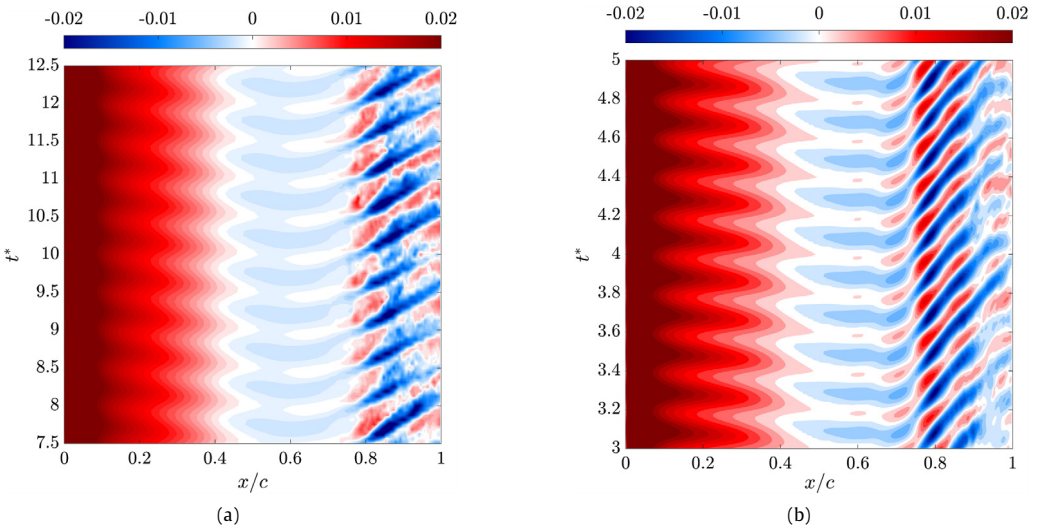

Fig. 17. Space–time diagram of instantaneous spanwise-averaged C_f: (a) $V_{f^+} = 2$; (b) $V_{f^+} = 5$.

the convection speed of $U_c = 0.43$, the distance between successive vortices is 8.6% of c, so 2 vortices easily fit in the region $x/c = [0.75 - 0.9]$.

The fact that the spatial structure that forms at this frequency is similar to that of the characteristic shear layer frequency (seen in Section 3.2) suggests that the periodic actuation is reinforcing a naturally occurring structure. This was a concept that was postulated by Benard and Moreau (2011) who suggested that the actuation acts as a catalyzer to amplify flow structures that already exist is the natural (i.e. unactuated) flow.

The phase-averaged plots reveal that once the flow has developed over the actuated airfoil, LCS are produced during every actuation cycle. This is consistent with the skin friction plots shown in Fig. 10 and suggest that the shear layer is 'locked-on'

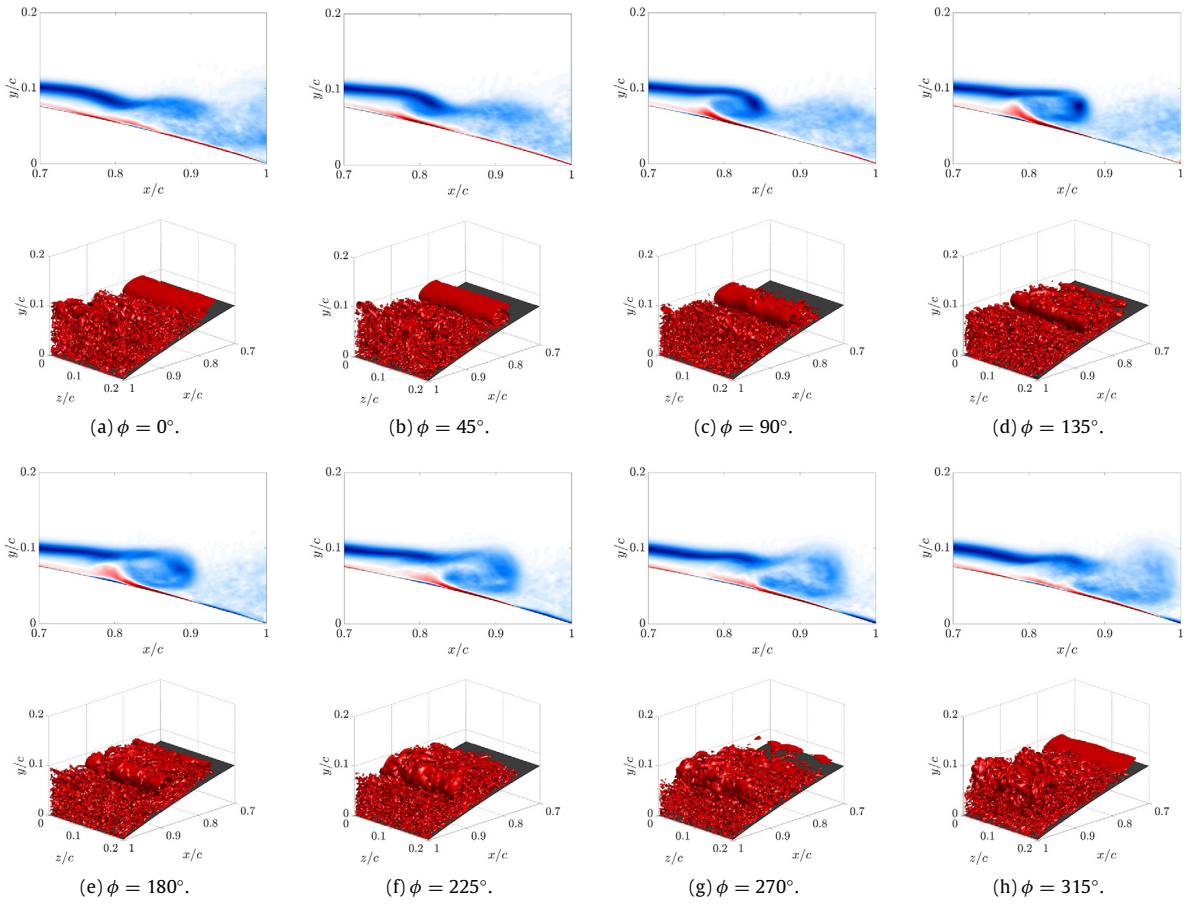

Fig. 18. Spanwise-averaged Ω_z (Top) and Q-criterion (Bottom) phase-averaged over 10 actuation cycles when $V_{f+} = 2$.

to the surface motion. The lock-on of the shear layer to the forcing frequency was also observed by Kotapati et al. (2010) in their investigation of synthetic-jet based periodic control.

The following mechanism is then proposed: the triggering of K–H instability is the first in a chain of events that eventually leads to separation control. Amplification of the K–H instability causes the early onset of shear layer roll-up and the creation of LCS. By entraining fluid from the outer flow and re-energizing the separated region, these structures can form closer and closer to the airfoil surface with each actuation cycle. It takes at least 15 cycles for this process to complete. Once this happens, the structures are directly re-energizing the near-wall flow, that recovers enough energy to overcome the adverse pressure gradient. Consequently the separation zone is significantly reduced. This mechanism will be further explored in the following section.

4.3. Time-averaged results

The process of time-averaging a velocity field involves averaging the velocity components at fixed points in space (the cell centers). Since the dynamic simulations involve time-varying cell center positions, care must be taken in the time-averaging process (refer to discussion in Section 2.1). Quantities on the airfoil surface (such as C_P and C_f) can be time-averaged as usual since they are always stored at the same locations on the airfoil boundary, but flow fields can only be averaged in a region where the cell centers are stationary — or move by only a small velocity. The maximum cell center displacement from the unactuated position was shown in Fig. 5(a). A zoomed-in plot around the airfoil is shown in Fig. 20(a). The cell centers move a maximum of less than 0.3% of the chord, which corresponds to the maximum surface displacement in Fig. 4(b). While this is a relatively small displacement, the velocity gradients are high in this region. It is therefore not appropriate to perform time-averaging in the near wall region over much of the airfoil surface. However, the surface does not move for $x/c > 0.93$ (see the distribution of boundary displacement in Fig. 4(b)). Furthermore, as shown in Fig. 20(b), the diffusion of the grid motion does not affect the cells in this region, or downstream of it. Indeed, the maximum cell displacement in the region enclosed by the white square in Fig. 20(a) is less than 0.03% of the airfoil chord and this occurs at ($x/c = 0.9$, $y/c = 0.2$). It

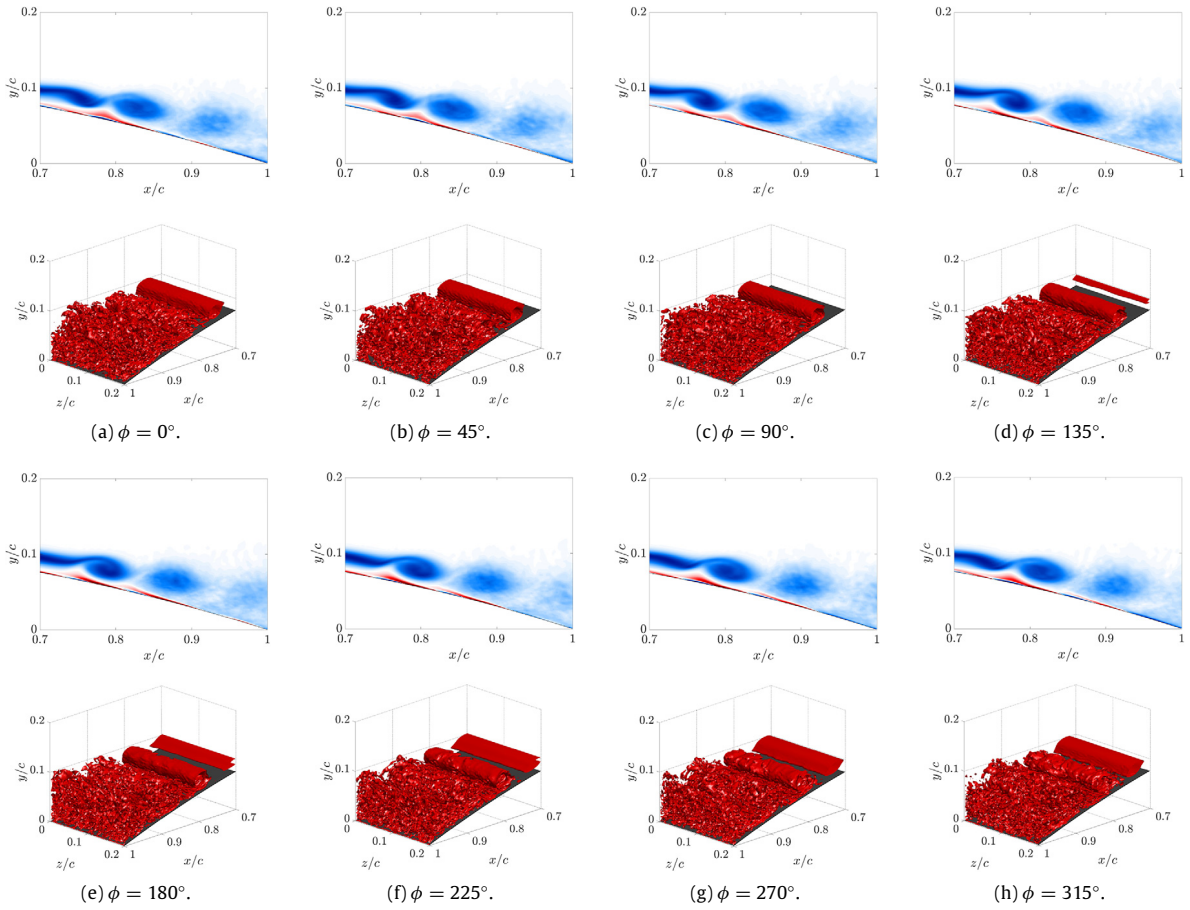

Fig. 19. Spanwise-averaged Ω_z (Top) and Q-criterion (Bottom) phase-averaged over 10 actuation cycles when $V_{f^+} = 5$.

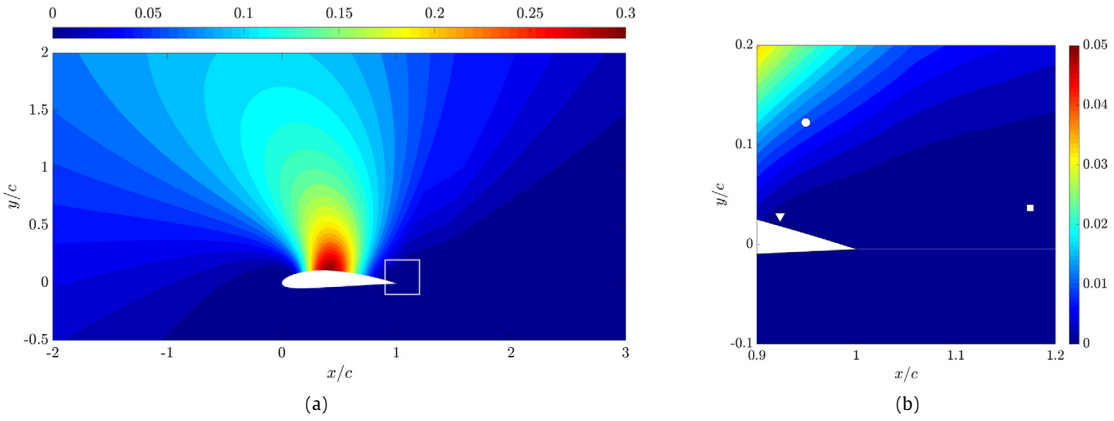

Fig. 20. Region close to the trailing edge, shown in (a) as a white square. This region has negligible grid motion (b)

is therefore appropriate to perform time-averaging in this small window. Thankfully, this is the area of most interest since it encompasses the majority of the reverse flow and the region of high TKE.

For the frequencies of $V_{f^+} = 2$ and 5, the time-averaging was performed using 80 snapshots from the final 10 cycles (i.e. 8 snapshots per cycle). Fig. 21 demonstrates that this number of samples is sufficient to provide a statistically converged time

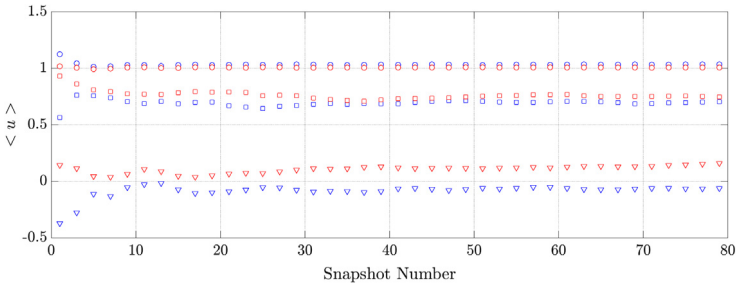

Fig. 21. Time-average streamwise velocity against the number of snapshots when $V_{f^+} = 2$ (blue) and $V_{f^+} = 5$ (red). The symbols correspond to the points shown in Fig. 20(b). (For interpretation of the references to color in this figure legend, the reader is referred to the web version of this article.)

Table 1
Aerodynamic force coefficients.

V_{f_+}	C_L	C_D	C_{D_p}/C_D	C_{D_v}/C_D
0	0.12	0.043	0.80	0.20
2	0.34	0.036	0.76	0.24
5	0.29	0.033	0.72	0.28

average for both actuation frequencies. The time-averaged streamwise velocity, TKE, and Reynolds stress, $\overline{u'v'}$, are shown in Fig. 22.

In Section 3.1 it was found that for the static airfoil, transition to turbulence occurred as a result of the natural breakdown of the separated shear layer. This means that the regions of high TKE and Reynolds stress occur in the shear layer, away from the airfoil surface. This can be seen in Fig. 22(a) where a clear gap between the region of high TKE and the airfoil surface is present. The mixing of momentum in regions of high TKE is well promoted but, since it occurs far from the airfoil surface and close to the trailing edge, it does not naturally cause reattachment in the airfoil surface. In the actuated cases shown in Fig. 22(b) and (c), the region of high TKE (high mixing of momentum) has been brought closer to the airfoil surface, enabling it to re-energize directly the boundary layer. This is consistent with the mechanism proposed in Section 4.2. Comparison of the streamwise velocity fields (mid and bottom row) with the unactuated time-averaged fields (top row) shows that this has caused a large reduction of the size of separated region at both frequencies and the reverse flow region, located at the trailing edge of the unactuated airfoil, has been significantly reduced. It can therefore be confirmed that dynamic surface motion at $V_{f^+} = 2$ and 5 is able to gradually move the region of high momentum transfer close to the airfoil surface. This then results in significant reduction in separation.

4.4. Effect of actuation on aerodynamic performance

The effect that actuation on the aerodynamic performance of the airfoil can be seen from the C_P distribution in Fig. 23. The time-averaging was performed over the same time periods as in the previous section (Section 4.3). It has already been mentioned in Section 3.1 that separation without reattachment in the unactuated case causes a flat C_P distribution, with a low pressure peak. From Fig. 23, dynamic surface actuation at $V_{f^+} = 2$ and 5 causes the pressure plateaux to be much shorter, terminating at $x/c = 0.76$ when $V_{f^+} = 2$ and 0.72 when $V_{f^+} = 5$ compared with $x/c = 0.93$ in the unactuated case. The improvement in pressure recovery over the aft portion of the airfoil allows for a larger negative pressure at the suction peak.

As can be seen in Table 1, this results in improvements in the aerodynamic force coefficients. When $V_{f^+} = 2$, C_L increases by 183% and C_D decreases by 32%. $V_{f^+} = 5$ has a greater decrease in C_D with a 37% reduction but the lift recovery is slightly less at 141%. This equates to a threefold L/D increase from 2.8 to 9.4 and 8.8 for $V_{f^+} = 2$ and 5 respectively. In both frequencies the flow is locked to the wall oscillation. Similar lift enhancement has been also observed when the motion of flexible membrane wings is synchronized with vortex shedding (Gordnier, 2009; Rojratsirikul et al., 2009).

The C_P plot indicates that frequency affects not only the pressure distribution on the suction side, but also the distribution on the pressure side. The combined effect results in the small drop in C_L and the ratio C_L/C_D when V_{f^+} increases from 2 to 5. It is not immediately evident how the top wall oscillation affects the pressure at the bottom wall. The effect is probably inviscid, because the flow is still attached in this area. It may be related to the periodic acceleration and deceleration of the mass adjacent to the moving wall, that has a global effect due to pressure coupling (continuity equation). The morphing wall covers 86% of the suction side, so a large mass is displaced. Interestingly, in the paper of Wang et al. (2015) the same behavior is also observed, when a small part of the wall in the suction side (close to the leading edge) is oscillating. In the lock-in region, the lift does indeed increase, but the increase is not monotonous and the authors do not report the ratio C_L/C_D. The pressure at the bottom wall is also affected by the motion.

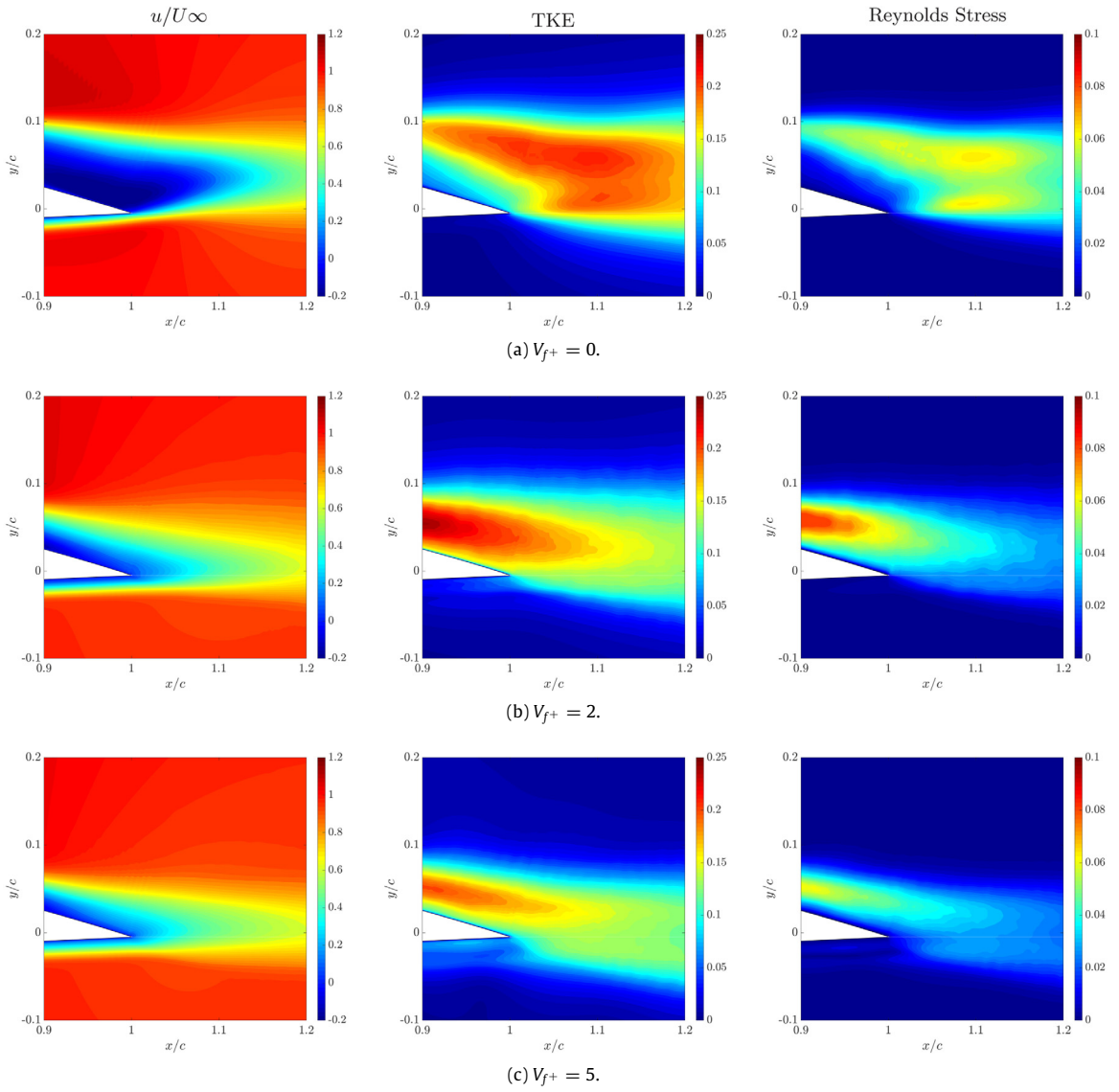

Fig. 22. Iso-contours of time-averaged flow fields close to the trailing edge for (a) $V_{f^+} = 0$; (b) $V_{f^+} = 2$; (c) $V_{f^+} = 5$. Left column $\overline{u}/U_\infty$; Mid column TKE; Right column Reynolds Stress.

Table 1 also shows a key advantage of this control method. Pressure drag, C_{D_p}, is the dominant drag component, which is expected since there is a large separated region. Passive methods attempt to reduce this by forcing the boundary layer to become turbulent upstream of the natural transition point. This keeps the boundary layer attached and hence reduces pressure drag. However, the viscous drag is substantially increased. Often the decrease in the C_{D_p} is greater than the associated increase in C_{D_v} and therefore a net reduction in C_D does occur. The particular control method examined in this paper does not rely on tripping the boundary layer. From Table 1 it can be seen that the contribution of pressure drag decreases and that of viscous drag slightly increases. The increase in the viscous component is a consequence of the increase in skin friction from the stronger vortex shedding. In absolute terms however the pressure drag, C_{D_p}, is reduced by 20% and 31% for $V_{f^+} = 2$ and 5 respectively compared to the static case. There is an associated relatively small increase in viscous drag.

5. Conclusions

In this paper the effect of dynamic surface motion on the flow development around the airfoil was explored computationally. The flow separated from the airfoil surface, transitioned but did not reattach. Actuation frequencies were chosen

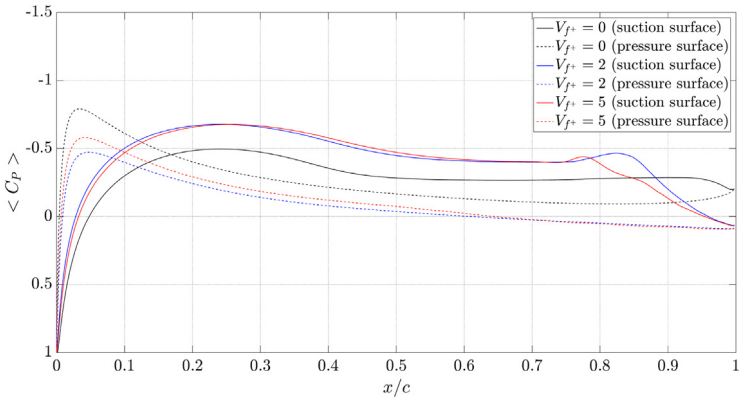

Fig. 23. Time- and spanwise-averaged C_P distributions over the actuated airfoil surface compared with the unactuated airfoil surface.

with reference to the fundamental shear layer frequency for the unactuated airfoil that originates from Kelvin–Helmholtz instability. It was found that after a few actuation cycles the Kelvin–Helmholtz instability was amplified and the shear layer started to roll-up earlier. LCS were formed in the shear layer which broke down and enhanced momentum transfer from the outer flow. As these were repeatedly formed and propagated downstream, the enhanced momentum transfer gradually impacted on the near-wall region. When these vortices were in direct contact with the near-wall region the flow became reasonably repeatable. The phase-averaged vorticity results demonstrated that the generation and shedding of the LCS was locked-on to the actuation frequency and the vortices were shed along the airfoil surface. Time-averaged plots of TKE and Reynolds stresses revealed that this resulted in the region of high momentum exchange occurring in the near-wall region, thus re-energizing directly the boundary layer. The overall result was an almost complete elimination of the separated regions and a significant improvement in aerodynamic performance.

Acknowledgments

The first author acknowledges financial support from the International Joint-Ph.D. Scholarship of the International Office of Imperial College. Significant financial assistance was also provided by Temasek Laboratories, National University of Singapore, Singapore. The simulations were carried out on the facilities of Archer, the UK national high-performance computing service, under the grant EP/L000261/1 of the UK Turbulence Consortium (UKTC) and on the High Performance Computing Service at Imperial College London (CX2).

References

Abbas, A., de Vicente, J., Valero, E., 2013. Aerodynamic technologies to improve aircraft performance. Aerosp. Sci. Technol. 28 (1), 100132.
Amitay, M., Smith, D.R., Kibens, V., Parekh, D.E., Glezer, A., 2001. Aerodynamic flow control over an unconventional airfoil using synthetic jet actuators. AIAA J. 39 (3), 361–370.
Benard, N., Moreau, E., 2011. On the vortex dynamic of airflow reattachment forced by a single non-thermal plasma discharge actuator. Flow Turbul. Combust. 87 (1), 1–31.
Brehm, C., Gross, A., Fasel, H.F., 2013. Open-loop flow-control investigation for airfoils at low Reynolds numbers. AIAA J. 51 (8), 1843–1860.
Buchmann, N.A., Atkinson, C., Soria, J., 2013. Influence of ZNMF jet flow control on the spatio-temporal flow structure over a NACA-0015 airfoil. Exp. Fluids 54 (3), 1–14.
Cattafesta, L.N., Sheplak, M., 2011. Actuators for active flow control. Annu. Rev. Fluid Mech. 43, 247–272.
Demirdžić, I., Perić, M., 1988. Space conservation law in finite volume calculations of fluid flow. Internat. J. Numer. Methods Fluids 8 (9), 1037–1050.
Dovgal, A., Kozlov, V., Michalke, A., 1994. Laminar boundary layer separation: Instability and associated phenomena. Prog. Aerosp. Sci. 30 (1), 6194.
Ferziger, J., Peric, M., 2002. Computational Methods for Fluid Dynamics, third ed. Springer-Verlag.
Gordnier, R., 2009. High-fidelity computational simulation of a membrane wing airfoil. J. Fluids Struct. 25, 897–917.
Gordnier, R., Chimakurthi, S., Cesnik, C., Attar, P., 2013. High-fidelity aeroelastic computations of a flapping wing with spanwise flexibility. J. Fluids Struct. 40, 86–104.
Greenblatt, D., Wygnanski, I.J., 2000. The control of flow separation by periodic excitation. Prog. Aerosp. Sci. 36 (7), 487–545.
Ho, C., Huerre, P., 1984. Perturbed free shear layers. Annu. Rev. Fluid Mech. 16, 365–422.
Horton, H., 1969. A semi-empirical theory for the growth and bursting of laminar separation bubbles. University of London, Queen Mary, Ph.D. thesis.
Issa, R.I., 1986. Solution of the implicitly discretized fluid flow equations by operator-splitting. J. Comput. Phys. 62, 40–65.
Jones, G., 2016. Control of flow around an aerofoil at low Reynolds numbers using periodic surface morphing. Imperial College London, Dept. of Aeronautics, Ph.D. thesis.
Jones, L.E., Sandberg, R.D., Sandham, N.D., 2008. Direct numerical simulations of forced and unforced separation bubbles on an airfoil at incidence. J. Fluid Mech. 602, 175.
Jones, G., Santer, M., Debiasi, M., Papadakis, G., 2017. Control of flow separation around an airfoil at low Reynolds numbers using periodic surface morphing. J. Fluids Struct. (submitted for publication).
Jovanovic, M., Schmid, P., Nichols, J., 2014. Sparsity-promoting dynamic mode decomposition. Phys. Fluid 26, 024103.

Kerho, M., Hutcherson, S., Blackwelder, R., Liebeck, R., 1993. Vortex generators used to control laminar separation bubbles. J. Aircr. 30, 315–319.
Kotapati, R., Mittal, R., Marxen, O., Ham, F., You, D., Cattafesta III, L., 2010. Nonlinear dynamics and sythetic-jet-based control of a canonical separated flow. J. Fluid Mech. 654, 65–97.
Laitone, E., 1997. Wind tunnel tests of wings at Reynolds numbers below 70,000. Exp. Fluids 23, 405–409.
Lin, J.C., 2002. Review of research on low-profile vortex generators to control boundary-layer separation. Prog. Aerosp. Sci. 38 (4), 389–420.
Marchman, J.F., Abtahi, A.A., 1985. Aerodynamics of an aspect ratio 8 wing at low Reynolds numbers. J. Aircr. 22, 628–634.
Marxen, O., Kotapati, R., Mittal, R., Zaki, T., 2015. Stability analysis of separated flows subject to control by zero-net-mass-flux jet. Phys. Fluids 27, 024107.
Marxen, O., Langs, M., Rist, U., 2013. Vortex formation and vortex breakup in a laminar separation bubble. J. Fluid Mech. 728, 58–90.
Mcmasters, J.H., Henderson, M.L., 1979. Low-speed single-element airfoil synthesis. In: NASA. Langley Res. Center the Sci. and Technol. of Low Speed and Motorless Flight, Part 1. NASA, pp. 1–31.
Mueller, T.J., Batil, S.M., 1982. Experimental studies of separation on a two-dimensional airfoil at low Reynolds numbers. AIAA J. 20, 457–463.
Mueller, T.J., DeLaurier, J.D., 2003. Aerodynamics of small vehicles. Annu. Rev. Fluid Mech. 35, 89–111.
Munday, D., Jacob, J., 2002. Active control of separation on a wing with oscillating camber. J. Aircr. 39, 187–189.
Postl, D., Balzer, W., Fasel, H.F., 2011. Control of laminar separation using pulsed vortex generator jets: direct numerical simulations. J. Fluid Mech. 676, 81–109.
Rhodes, O., Santer, M., 2012. Aeroelastic optimization of a morphing 2d shock control bump. In: 53rd AIAA Structures, Structural Dynamics and Materials Conference, Honolulu, Hawaii.
Rojratsirikul, P., Wang, Z., Gursul, I., 2009. Unsteady fluid-structure interactions of membrane airfoils at low Reynolds numbers. Exp. Fluids 46, 859–872.
Sato, M., Nonomura, T., Okada, K., Asada, K., Aono, H., Yakeno, A., Abe, Y., Fujii, K., 2015. Mechanisms for laminar separated-flow control using dielectric-barrier-discharge plasma actuator at low Reynolds number. Phys. Fluids 27 (11), 117101.
Schmid, P., 2010. Dynamic mode decomposition of numerical and experimental data. J. Fluid Mech. 656, 5–28.
Schubauer, G.B., Skramstad, H.K., 1948. Laminar-boundary-layer oscillations and transition on a flat plate. In: NACA Report 909. NACA, pp. 327–357.
Tani, I., 1964. Low-speed flows involving bubble separations. Prog. Aerosp. Sci. 5, 70–103.
Tu, J.H., Rowley, C.W., Luchtenburg, D.M., Brunton, S.L., Kutz, J.N., 2014. On dynamic mode decomposition: theory and applications. J. Comput. Dyn. 1 (2), 391–421.
Wahidi, R., Hubner, J.P., Zhang, Z., 2014. 3-D measurements of separated flow over rigid plates with spanwise periodic cambering at low Reynolds number. J. Fluids Struct. 49, 263–282.
Wang, W., Lei, P., Zhang, J., Xu, M., 2015. Effects of local oscillation of airfoil surface on lift enhancement at low Reynolds number. J. Fluids Struct. 57, 49–65.
Wang, S., Zhou, Y., Alam, M.M., Yang, H., 2014. Turbulent intensity and Reynolds number effects on an airfoil at low Reynolds numbers. Phys. Fluids 26 (11), 115107.
Wygnanski, I., Newman, B., 1964. The effect of jet entrainment on lift and moment for a thin airfoil with blowing. Aeronaut. Q. XV, 122.
Yarusevych, S., Sullivan, P.E., Kawall, J.G., 2009. On vortex shedding from an airfoil in low-Reynolds-number flows. J. Fluid Mech. 632, 245–271.
Zhang, W., Samtaney, R., 2015. A direct numerical simulation investigation of the synthetic jet frequency effects on separation control of low-Re flow past an airfoil. Phys. Fluids 27, 055101.
Zhou, Y., Wang, Z.J., 2012. Effects of surface roughness on separated and transitional flows over a wing. AIAA J. 50 (3), 593–609.